Research Article

Lingyu Zhao, Xiangchun Chang*, Dejiang Li, Junjian Zhang, Veerle Vandeginste, Peng Yao, and Jitong Su

Effect of coal facies on pore structure heterogeneity of coal measures: Quantitative characterization and comparative study

https://doi.org/10.1515/geo-2022-0738
received September 04, 2024; accepted November 11, 2024

Abstract: Coal facies is an important indicator reflecting depositional environment of coal, which affects pore distribution. The effect of coal facies on the nanopore structure is essential for deep coalbed methane drainage. In this study, 13 coal samples from the Upper Triassic Talichik Formation in the Kubei-Bashi tectonic belt were collected. The coal facies type is determined based on the coal phase parameters (TPI–GI diagram). On this basis, nanopore diameter distribution is determined by using liquid nitrogen adsorption and CO_2 adsorption experiments. Then, single and multi-fractal dimensions are studied by using fractal theories. The results are as follows. The coal facies are classified into three types, namely low swampy reed phases (Type A, GI > 5, TPI < 1), wetland herbaceous swamp phases (Type B, GI < 5, TPI < 1), and dry forest swamp phases (Type C, GI < 1, TPI > 1). The pore volume percentage of micropores is similar amongst the three facies types, showing that the coal facies has little effect on the pore structure of micropores. The pore volume and specific surface area of mesopores are the largest for coal facies *A*, indicating the most developed meso-pores in coal facies *A*. However, the pore volume percentage with a diameter of 2–10 nm in coal facies *A* is the lowest among the three coal facies. Above all, the coal reservoir under the wet overlying water depositional environment of coal facies *A* offers a relatively large pore volume as well as a specific surface area, which is more favorable for the exploration and development of coalbed methane; therefore, it is the advantageous coal reservoir in the study area.

Keywords: nanopore structure, fractal, coal facies, heterogeneity, Tarim Basin

1 Introduction

Coal facies exerts an important control on the pore characteristics of coal reservoirs, serving as a crucial indicator that reflects the coal depositional environment. The coal facies type imposes constraints on the scale of coal-bearing gas formation and productivity potential. Coal facies research has emerged as a hot topic in coal geology research [1–3]. Several researchers have studied pore characteristics through methods such as high-pressure mercury injection (HPMI) and low-temperature liquid nitrogen tests (LPN_2 GA). They have explored the intrinsic relationship between coal facies and pore characteristics, revealing variations in pore characteristics across different coal facies types [4,5].

Coal reservoirs represent heterogeneous porous media, and the morphology of pores and the structure of coal directly affect the physical properties of coal, as well as the adsorption–desorption and seepage characteristics of gas in the coal reservoir [6–8]. The pore structure dictates the gas content of coalbed methane and impacts the recoverability of coalbed methane [9–11]. The factors affecting the pore-fracture structure include the industrial components of coal rock, the degree of coal metamorphism, and the coal rock components [12,13]. However, the fundamental reason lies in the diversity of coal facies types, i.e., different depositional environments in which the coal reservoirs are

* **Corresponding author: Xiangchun Chang**, College of Earth Science and Engineering, Shandong University of Science and Technology, Qingdao 266590, China; Laboratory for Marine Mineral Resources, Qingdao National Laboratory for Marine Science and Technology, Qingdao 266071, China, e-mail: xcchang@sdust.edu.cn
Lingyu Zhao, Junjian Zhang, Peng Yao, Jitong Su: College of Earth Science and Engineering, Shandong University of Science and Technology, Qingdao 266590, China
Dejiang Li: Research Institute of Petroleum Exploration and Development, PetroChina, Beijing 100083, China; Key Laboratory of Gas Reservoir Formation and Development, CNPC, Langfang, Hebei 065007, China
Veerle Vandeginste: Department of Materials Engineering, KU Leuven, Campus Bruges, Bruges, Belgium

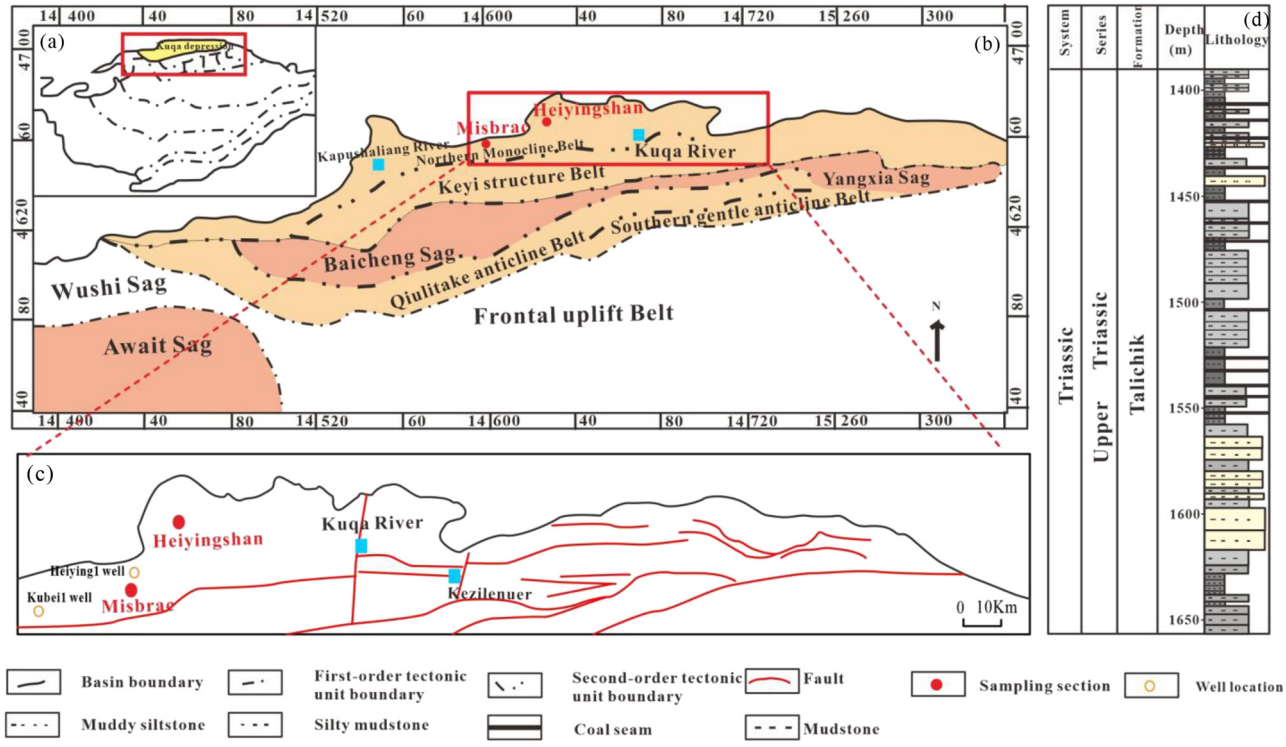

Figure 1: Study area location (a), tectonic unit division map of the Kuga Depression (b), sampling outcrop (c), and stratigraphic column of Triassic in northern Kuqa Depression (d).

located, with different coal facies types constraining the pore-fracture structure development.

Recent studies have employed fluid injection methods and image analysis techniques to provide detailed descriptions of the pore structure of coal reservoirs. In the context of adsorption reservoirs, the pore structure is a central factor affecting the gas content of the coal reservoir. Currently, the main methods for characterizing adsorbate pores include HPMI, LP N_2GA, CO_2 adsorption test (LP CO_2GA), and low-field nuclear magnetic resonance (LF-NMR) spectroscopy [14–16]. These methods are complemented by mathematical approaches such as fractal theory to quantitatively evaluate the heterogeneity of pore distribution [17,18]. For instance, Liu and Nie [19] utilized adsorption tests and image analysis approaches to analyze fractal characteristics, deriving pore distribution fractal dimension D_1 and surface fractal dimension D_2, effectively reflecting differences in pore distribution heterogeneity. Li et al. calculated pore volume fractal dimension D_v, surface fractal dimension D_s, and pore distribution fractal dimension D_p on the basis of FHH fractal theory and the Menger sponge model, providing quantitative evaluations of coal reservoir heterogeneity. Despite extensive studies by previous authors on coal facies division and the quantitative characterization of pore-fracture structure, few have delved into the impact of coal facies on the pore-fracture structure of reservoirs. Moreover, the impact of coal facies on the heterogeneity of pore-fracture distribution, crucial in reflecting the depositional environment of coal, remains largely unexplored [20].

This study focuses on coal samples collected from the Triassic Talichik Formation in the Misbrak and Heiyingshan sections, serving as representative samples. The identification of coal facies is based on the maceral characteristics. Quantitative characterization of the nanopore size distribution in coal samples is accomplished through LPN_2 GA and LPCO_2 GA tests. Subsequently, the pore structure characteristics of micropores and mesopores of different coal facies samples are discussed. Building upon these results, the heterogeneity of pores distribution is investigated using single and multiple fractal models. This article concludes by shedding light on the pore development mechanism.

2 Study area and experimental methods

2.1 Geological setting

The study area is situated within the Kubei–Bashi tectonic belt, located in the northern part of the Kuqa depression at

the northern margin of the Tarim Basin. It extends from the Kapshalyan River in the west to the Kuqa River in the east and from the Krasu Tectonic Belt in the south to the northern edge of the basin, covering an area of about 1,700 km^2 (Figure 1). The Kubei–Bashi tectonic zone is mainly controlled by a series of thrust faults, with its main body formed during the Neogene. Nevertheless, evident tectonic activities were also observed during the late Yanshan period. Overall, the thrust structure involves a complex basement. In the north, the Triassic strata are eroded to the surface, leading to the development of a series of gentle anticlines in the south, characterized by strong structural deformation [21].

The current stratigraphy revealed by outcrops and drilled wells in the study area primarily consists of Mesozoic–Cenozoic formations, with the Middle Jurassic Kyzylnur Formation and the Upper Triassic Talichik Formation identified as coal-bearing strata. During the period of coal seam development, the geological activities in the Southern Tianshan region were relatively stable, resulting in a limited impact of geological movements on changes in the depositional environment. Climate during this time largely regulated the depositional environment in the Kubei–Bashi tectonic belt [22]. The 13 coal samples in this study were mainly collected from the Upper Triassic Talichik Formation in the Misbrak section and Heiyingshan section in the Kubei–Bashi area, where fluvial and lacustrine depositional systems were prevalent during the depositional period of the Talichik Formation.

2.2 Experimental methods and computational theory

2.2.1 Experimental methods

The first step involved the microscopic identification of coal rock components based on the color, morphology, and structure of the coal samples. Then, the maceral analysis of the light section, prepared after crushing the coal seam, was carried out. The pulverized coal light sheet was examined under a reflective polarizing microscope using single polarization or incomplete orthogonal polarization. Accurate identification of macerals and minerals was achieved through quantitative analysis employing the number point method, as outlined in GB/T 8899 “Methods for Determination of Microscopic Components and Minerals of Coal.” Following this, the coal samples were ground into powdered form, and the vitrinite reflectance value ($R_{o,\ max}$) was measured using a microspectrophotometer. Finally, the coal samples were placed in a 40–60 mesh sieve to grind 6–10 g for subsequent analytical testing.

In this study, we focus on the pore characteristics (2–100 nm) of adsorption pores in coal reservoirs. According to the IUPAC pore classification method, pores with diameters of 0.4–2 nm are considered micropores, and pores with diameters of 2–100 nm are considered mesopores. The characterization of micropore structures involved the $LPCO_2$ GA test, whereas the LPN_2 GA test was employed for the characterization of mesopore structures.

2.2.2 Classification of coal facies

Various coal facies samples have been proposed in previous studies, forming the basis of classical coal facies research methods. Parameters, such as gelatinization index (GI), tissue preservation index (TPI), vegetation index (VI), groundwater index (GWI), vegetation index (VI), vitrinite/inertinite ratio (V/I), along with graphical analytical methods, such as TPI–GI phase diagrams and VI–GWI phase diagrams, have been popularly cited [23,24].

The more commonly cited methods for coal facies analysis include TPI, GI, VI, GWI, and GI–TPI phase diagram [25]. Upon the development and improvement of the calculation method, the formulae are as follows:

(1) TPI = (telinite + colotelinite + semifusinite + fusinite)/(colodetrinte + macrinite + inertodetrinite)
(2) GI = (vitrinite + macrinite)/(semifusinite + fusinite + inertodetrinite)
(3) GWI = (gelinite + corpogelinite + minerals + vitrodetrinite)/(telinite + telocolinite + colodetrinite)
(4) VI = (colotelinite + fusinite + semifusinite + suberinite + resinite)/(colodetrinite + inertodetrinite + alginite + liptodetrinite + sporinite + cutinite)

GI reflects the ratio of gelation products to non-gelation products. It can not only indicate the characteristics of water level changes in ancient peat bogs but also reflect the extent to which plant remains have been subjected to gelatinization. TPI represents the ratio of structural microscopic components to unstructured microscopic components in the vitrinite and inertinite, reflecting the degree of the well-preserved plant cell structure and the intensity of plant tissue degradation. GWI and VI signifies the degree of gelation of the fabrics depending on pH conditions [23,24].

2.2.3 Single-fractal model

The Frenkel–Halsey–Hill (FHH) model is the most widely used single-fractal model for analyzing liquid nitrogen test

Table 1: Maceral contents and industrial analysis results of coal samples

Section	Sample no.	$R_{o,max}$ (%)	Vitrinite (%)	Exinite (%)	Inertinite (%)	Mineral matter (%)	M_{ad} (%)	A_{ad} (%)	V_{daf} (%)	FC_{ad} (%)
	M-1	1.31	89.14	0	8.99	1.87	0.86	7.10	24.89	69.78
	M-2	1.23	87.01	0	11.42	1.57	0.80	2.96	25.88	71.93
	M-3	1.11	45.75	0	7.08	47.17	1.25	51.84	30.72	33.37
	M-4	1.19	91.04	0	1.08	7.88	0.65	18.98	23.43	62.03
	M-5	1.19	56.54	0	7.01	36.45	0.45	22.68	40.09	46.32
Misbrak	M-6	1.21	76.95	0	9.66	13.39	0.82	2.66	22.33	75.60
	M-7	1.17	56.06	0.76	18.94	24.24	0.92	5.08	27.89	68.45
	M-8	1.08	51.58	6.66	41.06	0.7	0.70	4.11	26.93	70.07
	M-9	1.42	58.65	0	25.56	15.79	0.86	41.56	22.59	45.24
	M-10	1.11	70.86	0	26.98	2.16	0.94	22.92	25.16	57.69
	H-1	0.70	33	6.27	59.08	1.65	1.31	3.65	33.40	64.17
Heiyingshan	H-2	0.82	33.61	1.66	56.43	8.3	2.06	39.45	38.55	37.21
	H-3	0.71	21.89	0.38	75.09	2.64	0.96	1.60	34.76	64.20

data [26]. Fractal values in this model are mainly obtained by linear fitting of adsorption and relative pressure. This fractal model can provide a detailed analysis of pore heterogeneity in the pore size range of 2–100 nm, with the fractal dimension calculated as follows:

$$\ln\left(\frac{V}{V_0}\right) = C + A\left\{\ln\left[\ln\left(\frac{P}{P_0}\right)\right]\right\}, \quad D = 3A + 3, \quad D = A + 3. \tag{1}$$

Here, V is the adsorption volume corresponding to the equilibrium pressure P, $cm^3\,g^{-1}$; C is a constant; V_0 is the

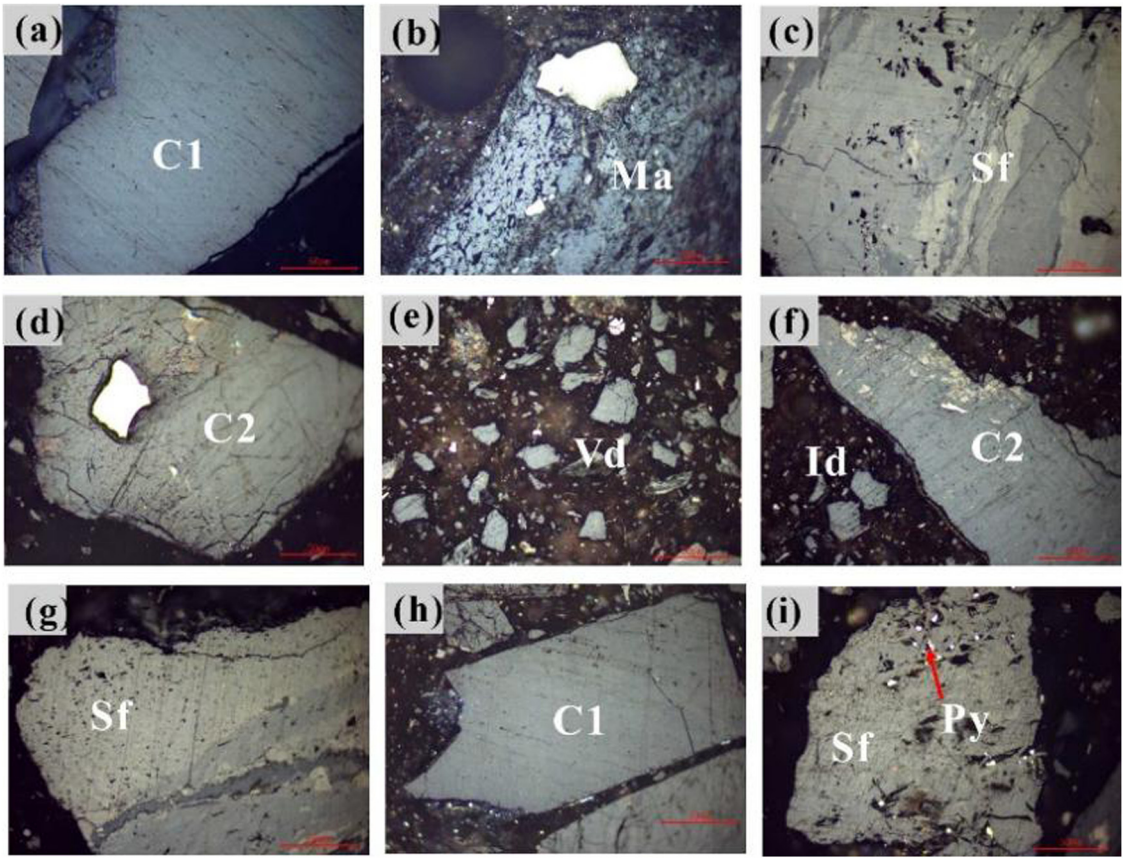

Figure 2: Maceral photomicrographs. (a) M-2, telocollinite (C1), (b) M-3, macrinite (Ma), (c) M-6, semifusinite (Sf), (d) M-7, desmocollinite (C2), (e) M-10, vitrodetrinite (Vd), (f) M-10, inertodetrinite (Id) and desmocollinite (C2), (g) H-1, semifusinite (Sf), (h) H-2, telocollinite (C1), (i) H-3, semifusinite (Sf) and pyrite (Py).

adsorption volume of the monomolecular layer of gas, $cm^3\ g^{-1}$; P_0 is the saturated vapor pressure, MPa; and A is the power law index, and its value is controlled by the fractal dimension (D), where a larger value of D indicates stronger pore heterogeneity.

Based on the CO_2 adsorption test results, the fractal model was used to study the heterogeneity of micropores. The equation can be expressed as

$$\ln S_r = \ln(S_0 K_s) + C \ln r, \quad (2)$$

where S_r is the cumulative specific surface area, $m^2\ g^{-1}$; r is the pore radius, nm; and D is the fractal dimension, dimensionless; surface fractal dimension $D = 2 + C$ or $D = (C - 3)/3$. A larger D value indicates stronger heterogeneity of pores.

2.2.4 Multi-fractal model

Multiple fractal allows for a more detailed characterization of the complexity and heterogeneity of the sample. For reservoirs with strong heterogeneity, such as coal reservoirs, the pore size distribution curve will not only fluctuate but also jump randomly. In addition, different pore spacing parts are similar, making multifractals advantageous for calculating nanopore distribution heterogeneity [27,28]. Multifractal calculation results include two forms from previous studies, i.e., a~f (a) singular and q~D fractal dimension spectrum. It can be concluded that the two forms have an explicit correlation [29]. Therefore, in this study, the q~D fractal dimension spectrum is selected to describe the multifractal results of coal samples. The formula is as follows:

$$u(q, \varepsilon) = \sum_{i=1}^{N(\varepsilon)} P_i(\varepsilon)^q \sim \varepsilon^{\tau(q)}, \quad (3)$$

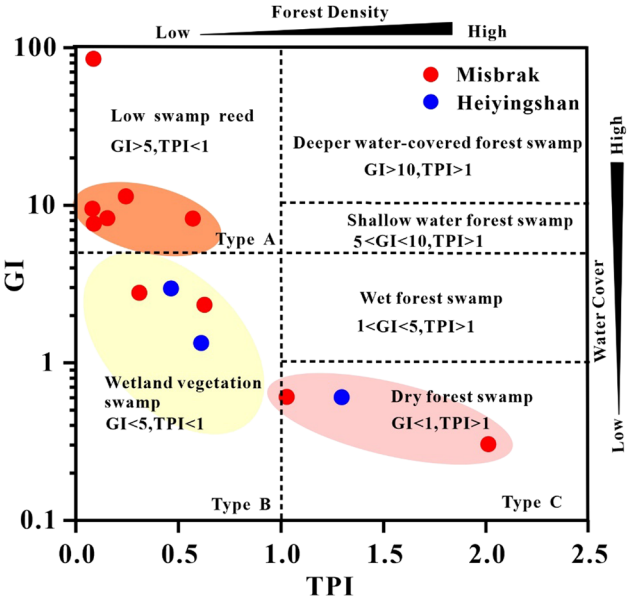

Figure 3: Classification of coal facies.

where q is the index representing the fractal characteristics of objects at different scales. τ_q is the q-order mass scale function and can be expressed as

$$\tau(q) = \lim_{\varepsilon \to 0} \left[\ln \sum_i P_i(\varepsilon)^q / \ln(1/\varepsilon) \right]. \quad (4)$$

Therefore, the generalized dimension (D_q) can be defined as

$$D_q = \tau(q)/(q - 1). \quad (5)$$

When $q = 1$, D_q becomes

Table 2: Coal facies division parameters

Section	Sample no.	$R_{o,max}$ (%)	TPI	GI	VI	GWI	V/I
	M-1	1.31	0.24	11.33	0.24	0.02	9.92
	M-2	1.23	0.57	8.22	0.58	0.02	7.62
	M-3	1.11	0.09	7.62	0.09	1.05	6.47
	M-4	1.19	1.03	0.61	1.00	0.26	0.60
Misbrak	M-5	1.19	0.63	2.33	0.63	0.28	2.29
	M-6	1.21	2.01	0.30	2.04	0.12	0.29
	M-7	1.17	0.09	84.67	0.09	0.09	84.67
	M-8	1.08	0.31	2.78	0.31	0.03	2.63
	M-9	1.42	0.08	9.46	0.08	0.66	8.07
	M-10	1.11	0.15	8.27	0.15	0.21	7.97
	H-1	0.70	1.30	0.60	1.18	0.05	0.56
Heiyingshan	H-2	0.82	0.47	2.96	0.46	0.53	2.96
	H-3	0.71	0.61	1.34	0.56	0.01	1.26

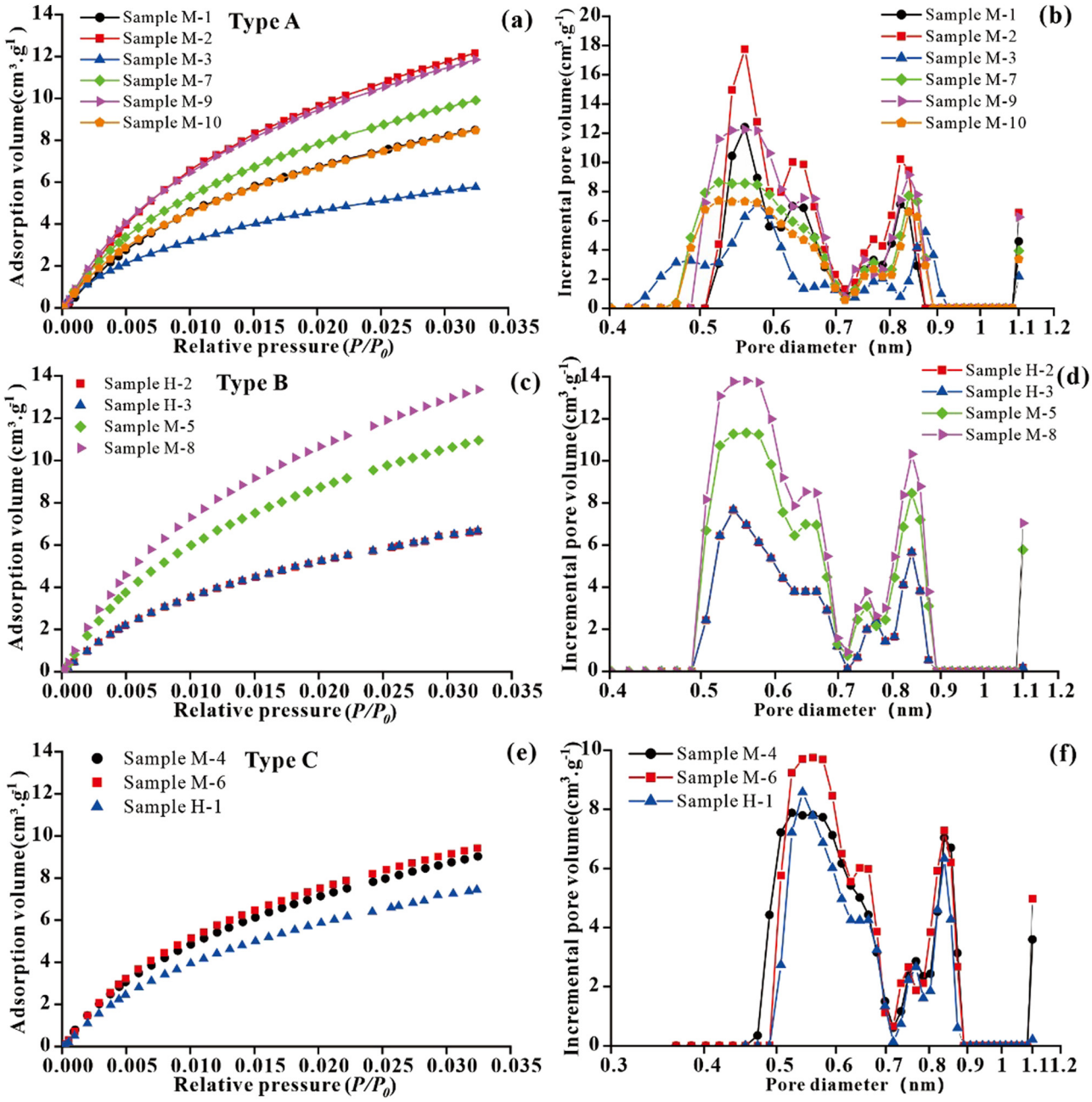

Figure 4: CO_2 adsorption curves of coal samples (a, c, e) and micropore distribution of different coal facies samples (b, d, f).

$$D_1 = \lim_{\varepsilon \to 0} \left(\sum_{i=1}^{N(\varepsilon)} p_i(\varepsilon) \ln p_i(\varepsilon) \right) / \ln(\varepsilon). \quad (6)$$

Relevant parameters include D_{min}, D_{max}, D_0, $D_0 - D_{max}$, and $D_{min} - D_0$. Multifractal results calculated from the adsorption data show that in the low-value zone of pore volume, a larger $D_{min} - D_0$ indicates a stronger heterogeneity in pore size distribution [30]. In the high-value zone of pore volume, increasing $D_0 - D_{max}$ indicates a stronger heterogeneity in pore size distribution.

3 Results and discussion

3.1 Coal sample characterization and coal facies classification

The results of the industrial analysis of the samples, as well as the maceral contents, are shown in Table 1. The macroscopic coal rock type in the study area is dominated by the semi-bright type, and $R_{o,max}$ of the coal samples in the

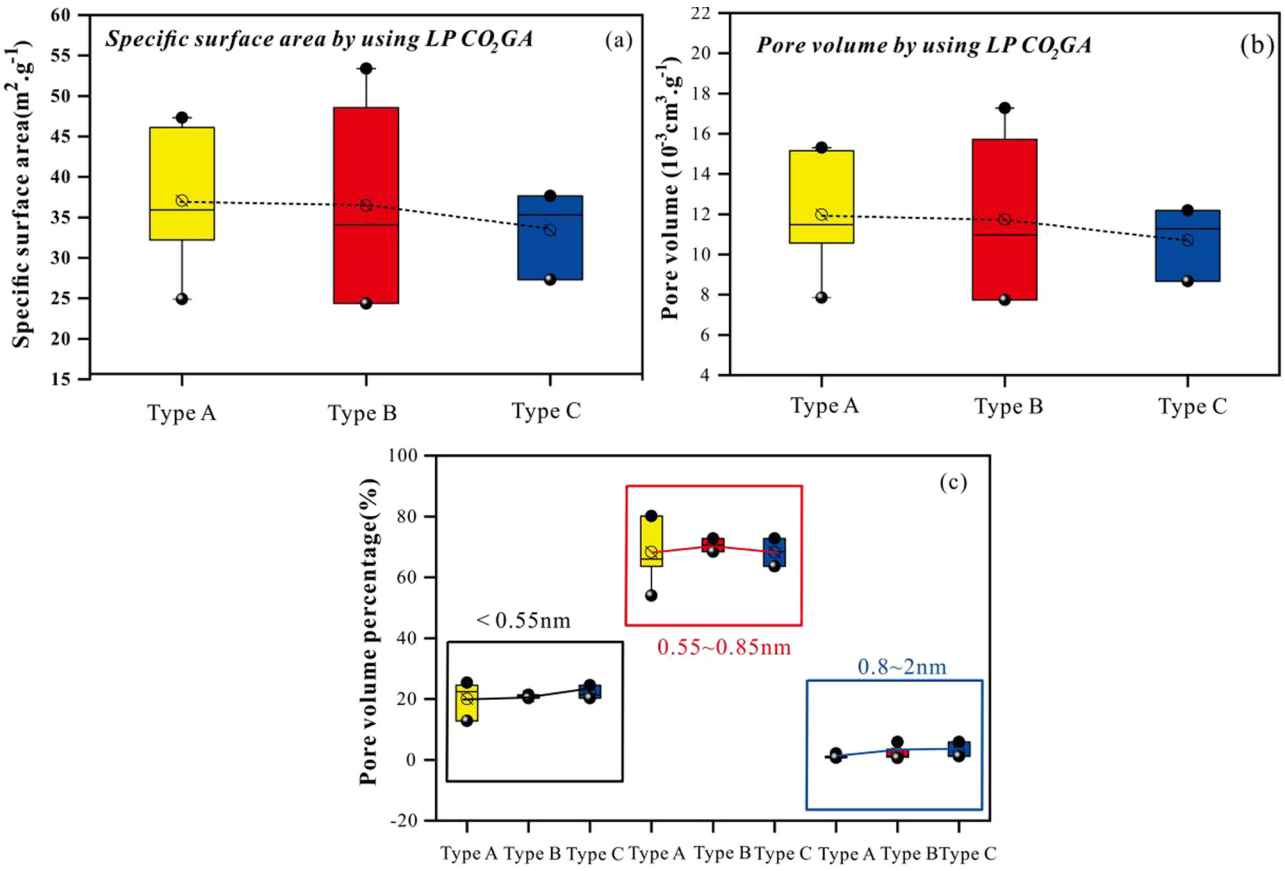

Figure 5: Comparison of structure parameters of micropores. Specific surface area of different coal facies types (a), pore volume of different coal facies types (b), and pore volume percentage of different coal facies types (c).

Misbrak section ranges from 1.08 to 1.42%, indicating a higher degree of thermal evolution (Table 1). The organic maceral group is predominantly composed of vitrinite, followed by inertinite, and negligible exinite content. Within the vitrinite maceral subgroup, desmocollinite is the predominant component, followed by vitrodetrinite and telocollinite. The inertinite maceral subgroup is primarily comprised of semifusinite, with minor amounts of macrinite and inertodetrinite (Figure 2). The $R_{o,max}$ of coal samples from the Heiyingshan section ranges from 0.70 to 0.82%, and the organic maceral group is dominated by inertinite and exhibits the lowest exinite content. The industrial analysis parameters indicate that all coal samples have the highest fixed carbon content, and the volatile content generally exceeds the ash and moisture content.

The coal samples selected for this study have similar maturity levels, classified as medium-rank coal (Table 1), with minimal structural variation. Analysis of submicroscopic component images and mineral content shows that the coal surface structure in the study area is smooth, containing clay minerals and pyrite. Coal reservoirs developed in coal facies *A* are rich in vitrinite, with well-developed micropores. The pyrite filling these micropores influences the pore structure development. In contrast, coal reservoirs in facies *B* and *C* have higher inertinite content, characterized by well-developed microfractures filled with clay minerals. Compared to Facies *A*, Facies *B* and *C* have less micropores development but more mesopores and macropores, with pore structure influenced by clay minerals. The observed mineral types in microphotographs align with descriptions from hand specimen analyses.

Table 2 shows the division parameters of coal facies. The TPI–GI diagram reflects the conditions of coal-forming plant swamp media and provides information about the depositional environment during peat aggregation. The coal facies are classified into three types based on TPI and GI, namely low swampy reed phases (Type A, GI > 5, TPI < 1), wetland herbaceous swamp phases (Type B, GI < 5, TPI < 1), and dry forest swamp phases (Type C, GI < 1, TPI > 1). Coal facies *A* is characterized by the highest GI and lowest TPI values, indicative of a wet overlying water depositional environment; coal facies *C* exhibits the lowest

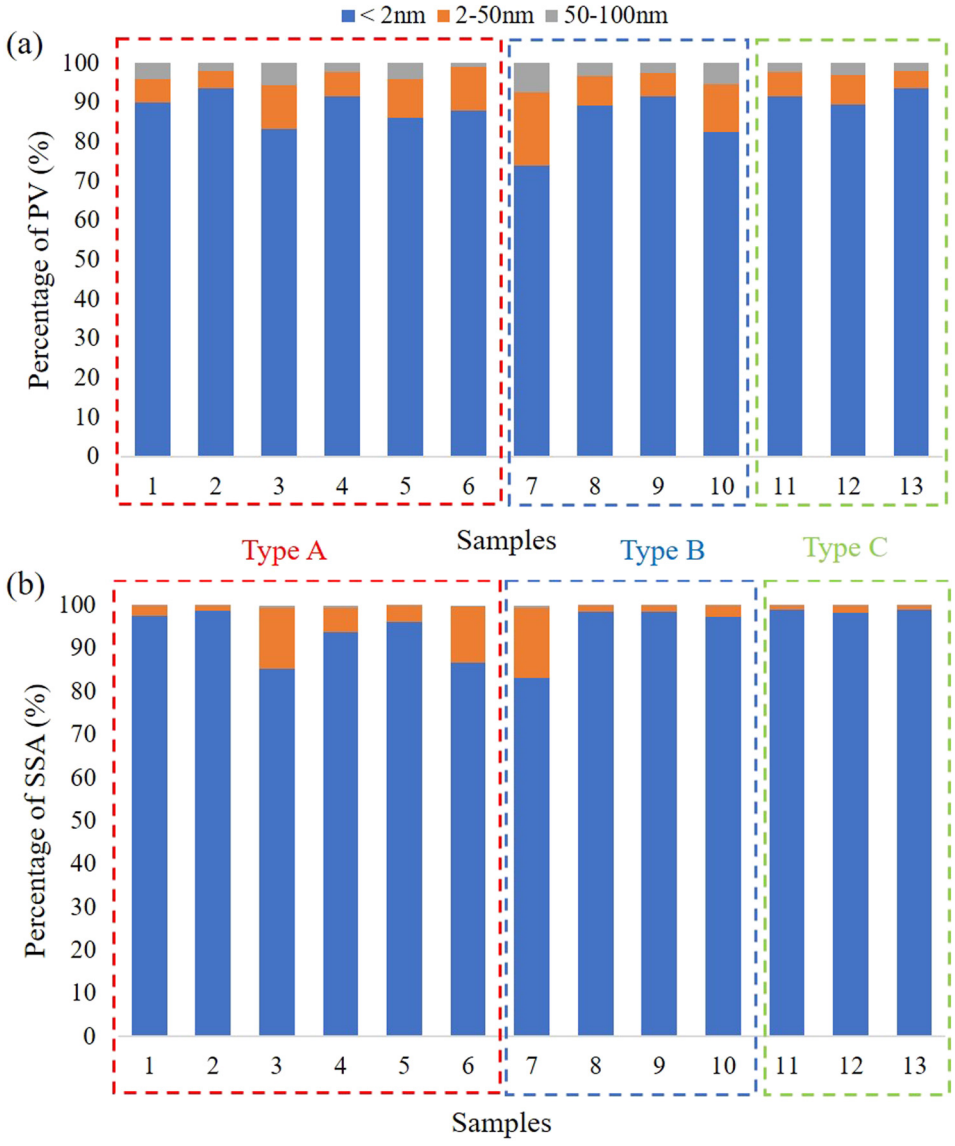

Figure 6: Distributions of the pores of different coal facies types: (a) the percentage of pore volume and (b) the percentage of specific surface area.

GI and highest TPI values, suggesting a dry depositional environment (Figure 3).

3.2 Effect of coal facies on 0.4–1.2 nm pore heterogeneity

3.2.1 Micropore distribution of samples with different coal facies types

The CO_2 adsorption curve reflects the pore size distribution of micropores. Figure 4a, c, and e show that the adsorption volumes of coal samples in coal facies *A*, *B*, and *C* are 5.77–12.15 $cm^3\ g^{-1}$, 6.64–13.35 $cm^3\ g^{-1}$, and 7.45–9.42 $cm^3\ g^{-1}$, respectively (Figure 4a, c, and e). The micropore distribution curves of all coal samples show two pore peaks at about 0.55 and 0.85 nm, respectively. The peak of the pore size distribution curves of coal facies *B* and *C* showed an inverted U-shape at 0.55 nm compared with that of coal facies *A*, which indicated that the pore size development is more homogeneous (Figure 4b, d, and f).

The volume and specific surface area of micropores are similar across three coal facies (Figure 5a and b), and also the pore volume percentage for the micropores of 0.40–0.55 nm, 0.55–0.85 nm, and 0.85–1.2 nm are similar among the three facies types (Figure 5c), showing that the coal facies types have little effect on the pore structures of micropores.

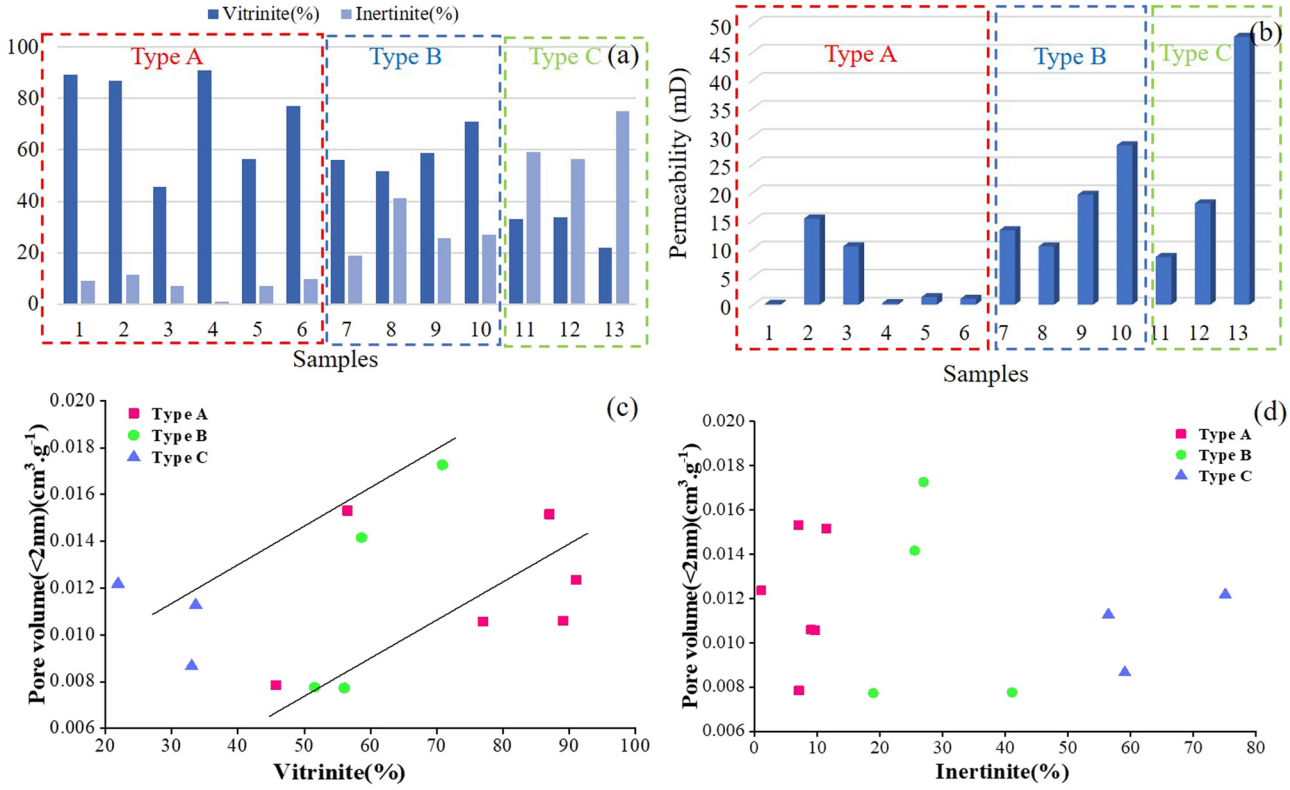

Figure 7: Vitrinite and inertinite content of different samples (a), permeability data (b), and the relationship between micropore volume and submicroscopic components (c and d).

Although the pore size distribution curves show some differences across coal facies types, the peak pore size distribution is similar among the different coal types. Generally, micropores contribute the majority of pore volume (averaging 88%), followed by mesopores (averaging 8%), with macropores contributing the least pore volume (averaging 4%) (Figure 6a). The distribution characteristics of specific surface area also vary across coal facies types. Micropores typically provide most of the specific surface area (averaging 95%), with mesopores contributing around 5% and macropores contributing a negligible amount (Figure 6b). This indicates that micropores are well-developed in deep coal reservoirs. The pore volume and specific surface area distribution trends are consistent across different coal facies types, as the pore size range aligns with the development of the specific surface area. Moreover, micropores play a dominant

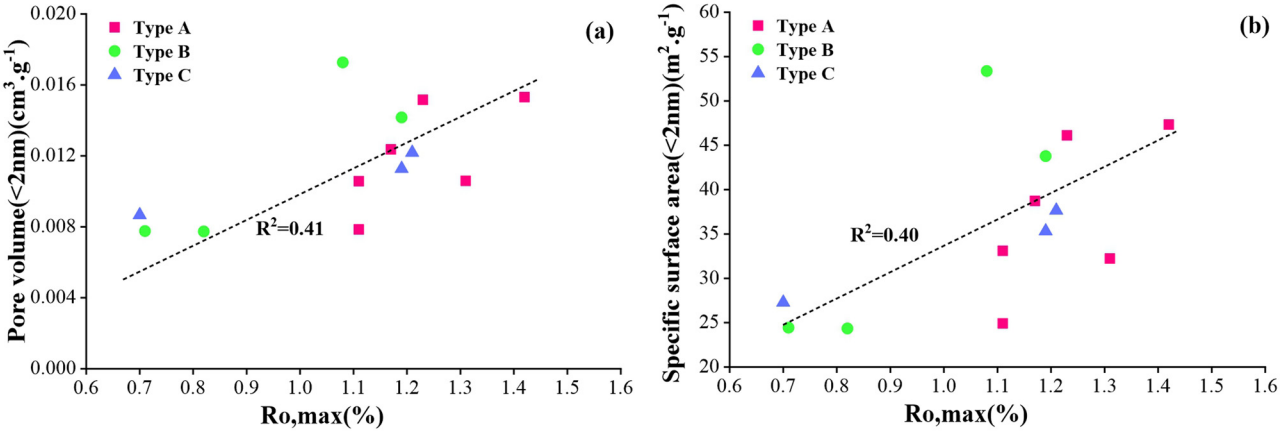

Figure 8: Relationship between micropore volume and $R_{o,\,max.}$. Crossplots of $R_{o,\,max.}$ and pore volume (a) and crossplots of $R_{o,\,max.}$ and specific surface area (b).

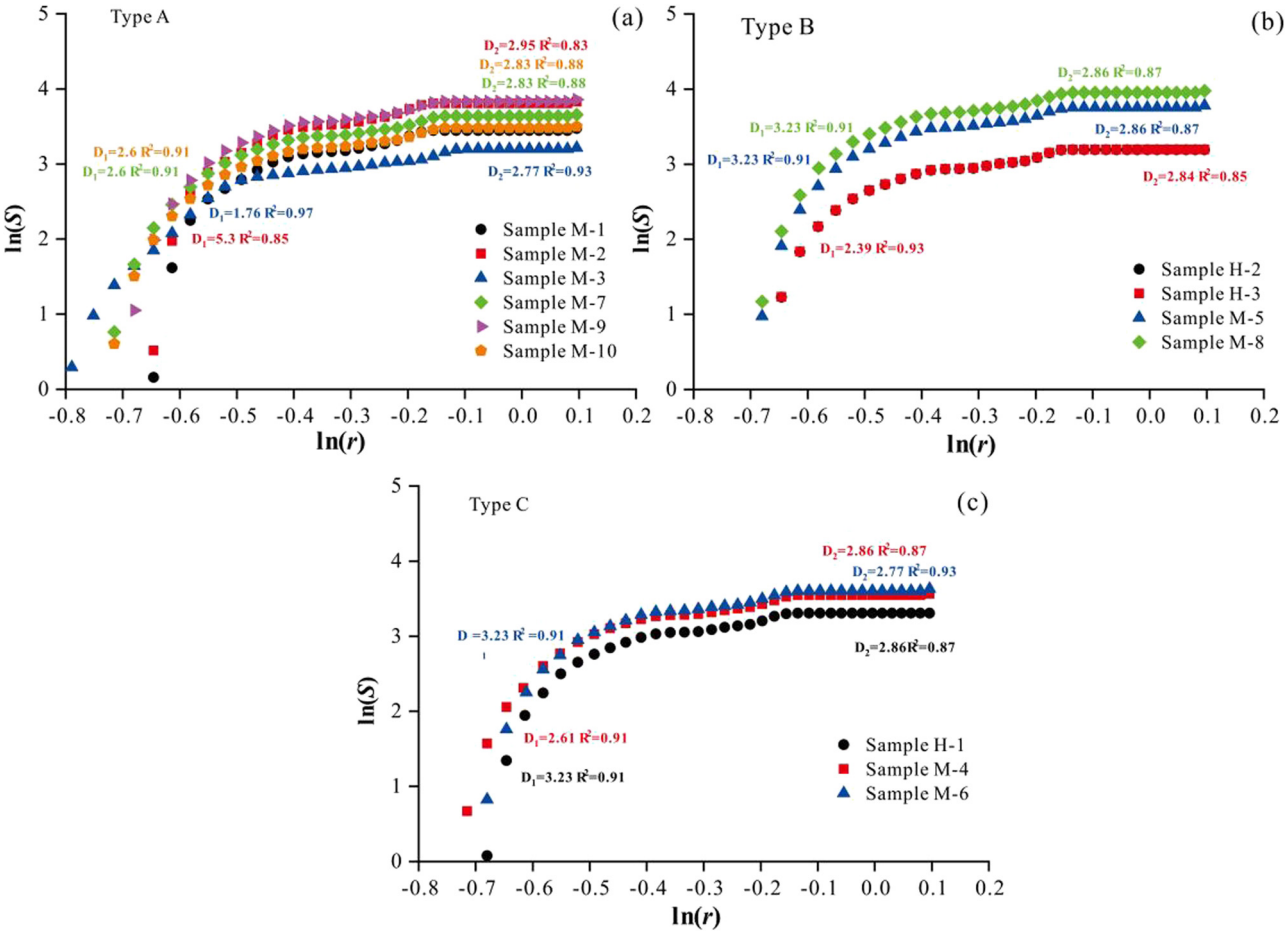

Figure 9: Fractal curves of micropore distribution. Single fractal curves of coal facies A (a), single fractal curves of coal facies B (b), and single fractal curves of coal facies C (c).

role in contributing to both pore volume and specific surface area, suggesting that the primary sites for coalbed methane adsorption and storage are micropores with high specific surface areas, which also serve as effective pathways for initial gas migration and diffusion after desorption.

Previous studies have found that exinite and inertinite contain fewer pores, whereas pores are well-developed in vitrinite, and the abundance of mineral pores is related to the types of minerals present in coal. Coal facies *A* is characterized by a high vitrinite content with well-developed

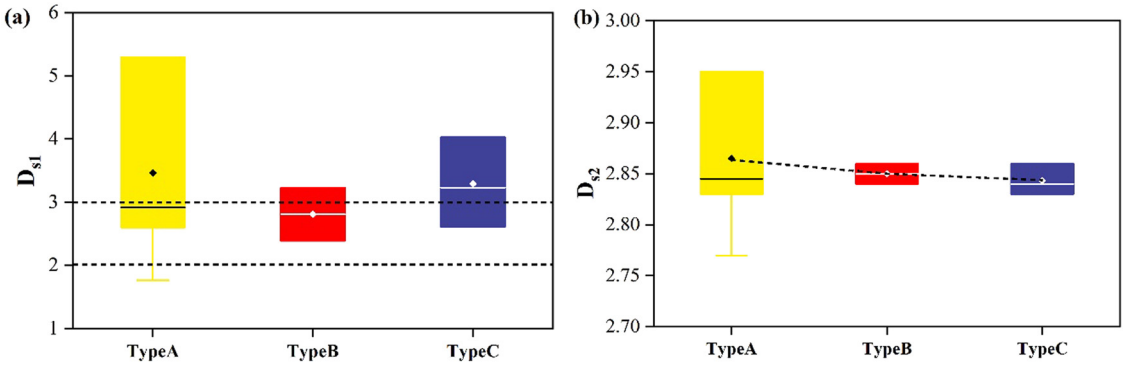

Figure 10: D_{S1} of different coal facies types (a) and D_{S2} of different coal facies types (b).

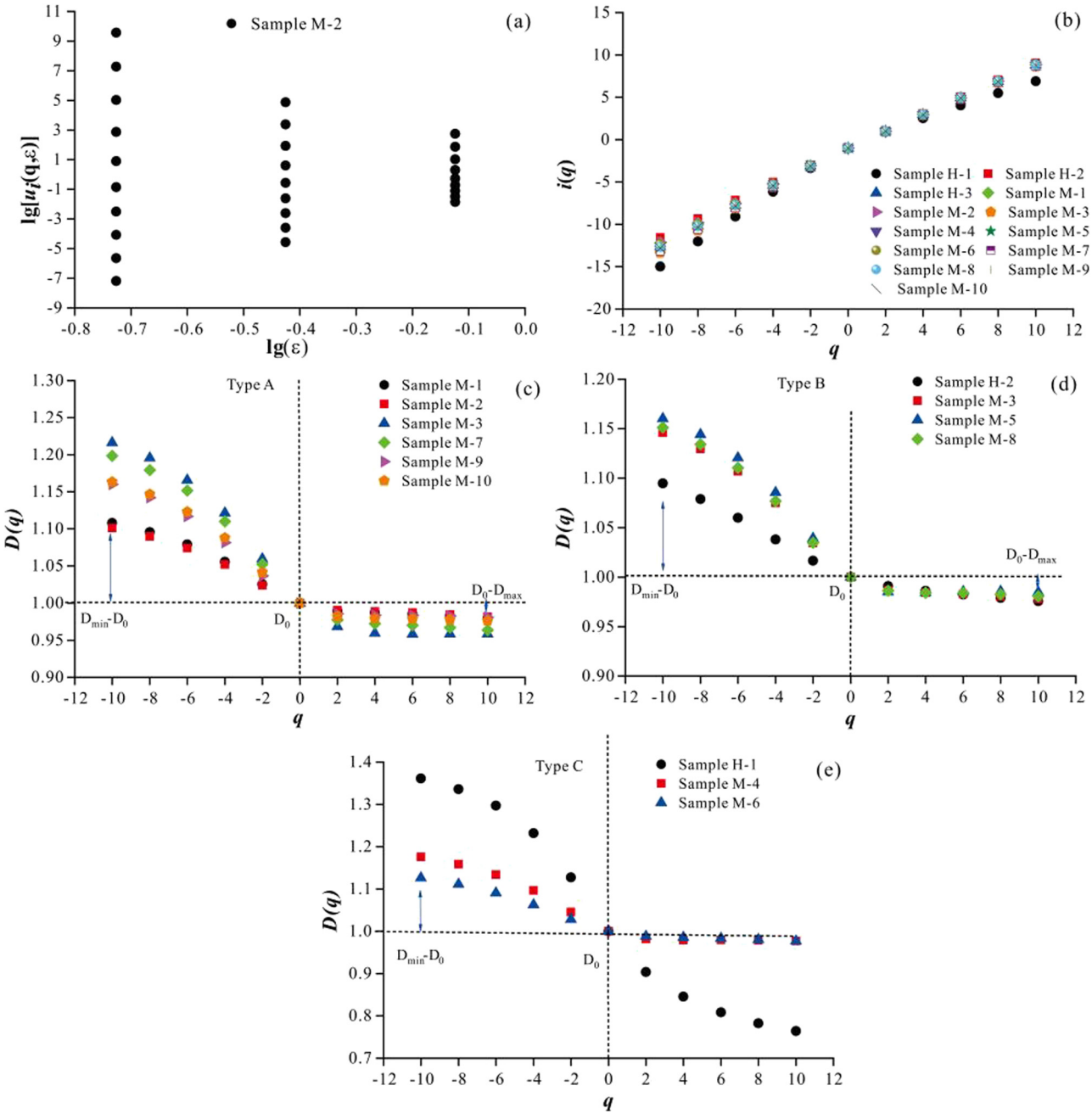

Figure 11: Multifractal curves characteristics of micropores. The linear relationship between *q* and *i(q)* (a, b), and the linear relationship between *q* and *D(q)* in different coal facies types (c–e).

micropores and relatively low permeability, whereas coal facies *C*, characterized by high inertinite content, exhibits more meso- to macropores and higher permeability (Figure 7a and b). Compared to inertinite, vitrinite shows a positive correlation with micropore volume, indicating that vitrinite plays a role in controlling micropore development (Figure 7c and d).

Figure 8 shows a strong positive correlation between $R_{o,max}$ of micropores, and both pore volume and specific surface area. As $R_{o,max}$ increases, the pore volume of each sample increases linearly, accompanied by an increase in specific surface area. This is primarily due to an increase in coal maturity, where macropores gradually decrease while micropores, such as adsorption pores, increase. The $R_{o,max}$ values for all samples range from 0.65 to 2%, classifying them as medium-rank coal. However, there are differences in $R_{o,max}$ values across different coal facies types: coal facies *A* has the highest average $R_{o,max}$ (average 1.23%). The samples from coal facies *A* also show the largest pore volume and specific surface area, consistent with the higher vitrinite content characteristic of this facies.

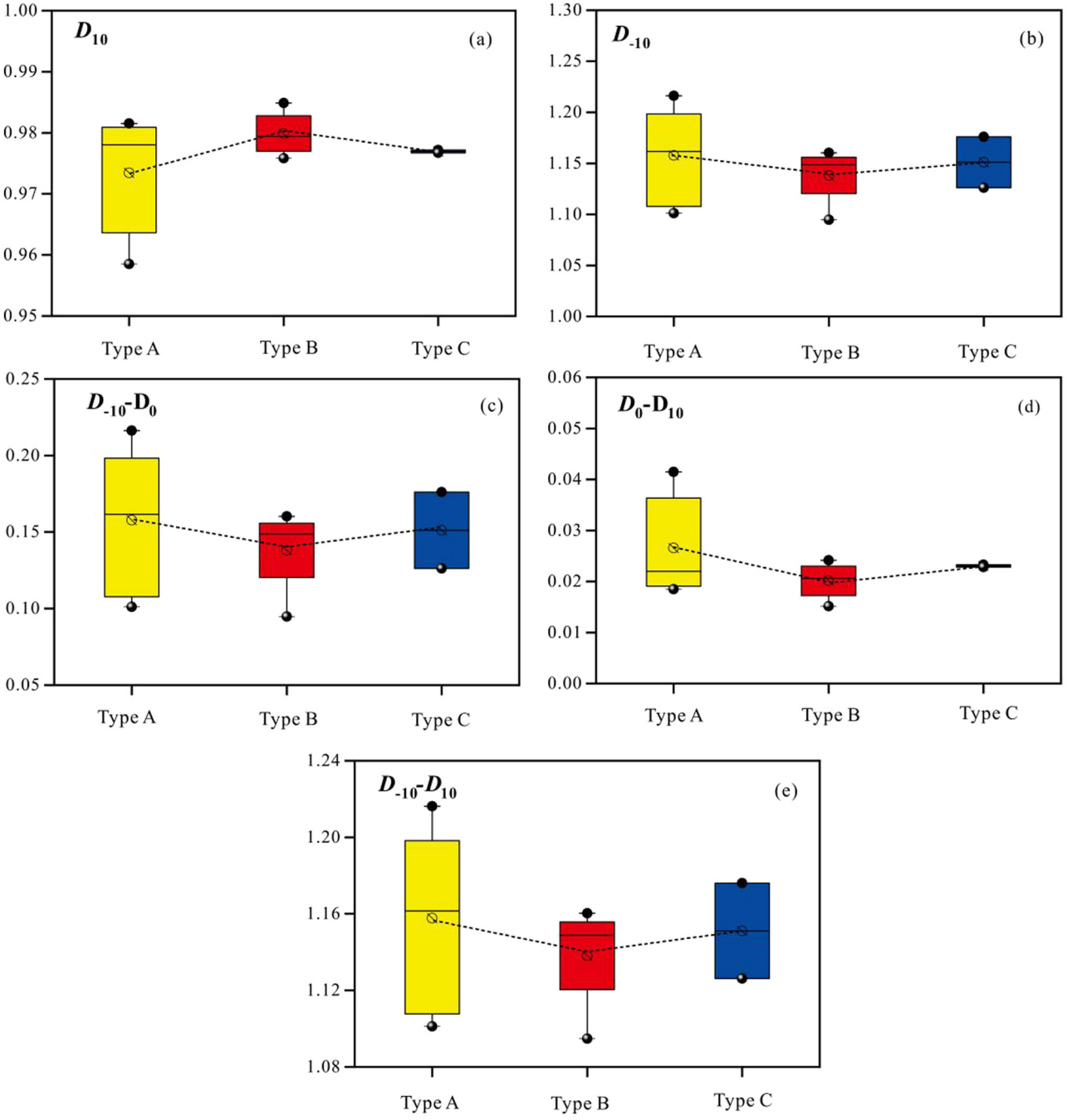

Figure 12: Comparison of multi-fractal characteristics between different coal facies types. D_{10} and D_{-10} of different coal facies types (a, b), the relationship between D_{10}, D_{-10} and D_0 (c–e).

3.2.2 Single-fractal analysis based on carbon dioxide adsorption curves

The micropore fractal characteristics are analyzed using the CO_2 adsorption data (Figure 9). The results indicate that there exist differences in the two segments of the single-fractal curve of micropores before and after the critical diameter, taken as 0.6 nm. This division illustrates the heterogeneity of the pore distribution for pores smaller than 0.4–0.6 nm and 0.6–2.0 nm.

The demarcation point of the fractal curve is approximately ln (r) = −0.5 (r = 0.60 nm), indicating significantly different fractal characteristics (Figure 9). Calculations confirm that this value corresponds to the position of peak 1 in Figure 4b, d, and f. Therefore, the fractal demarcation point is determined to be the average peak position of 0.60 nm. The

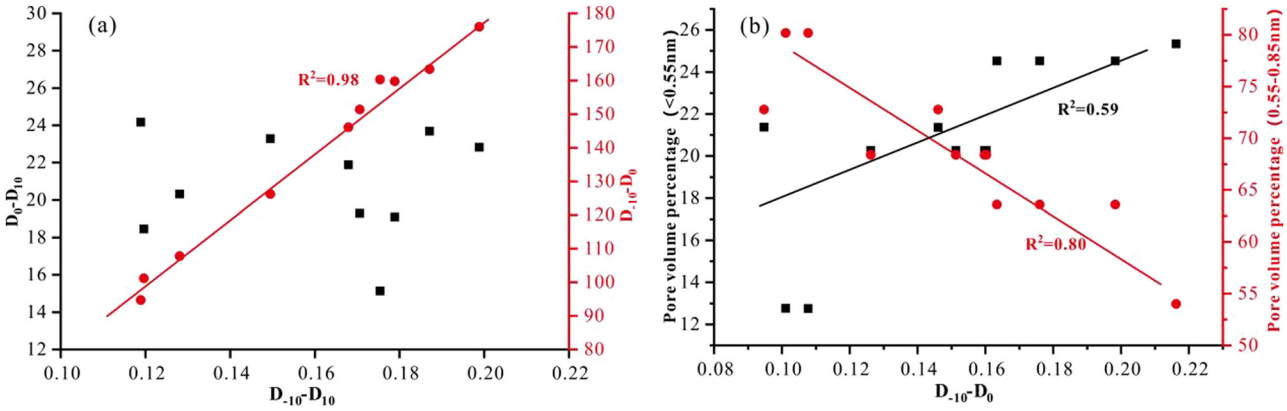

Figure 13: Relationship between multi-fractal and pore structure parameters. Plots of $D_{-10} - D_{10}$ and $D_0 - D_{10}$ (a), the relationship between $D_{-10} - D_0$ and pore structure parameters (b).

fractal dimension for each sample comprises two parameters, namely D_{s1} ($r < 0.6$ nm) and D_{s2} ($r > 0.6$ nm). The results show that D_{s1} ranges from 1.76 to 5.3 (Figure 10a), which falls outside the typical fractal range of D between 2 and 3 [30–32]. This deviation is primarily attributed to the limited pore data points in the range of 0.47–0.60 nm during the testing process, resulting in a calculation range of only 0.13 nm. To ensure accurate calculations, this section focuses in terms of fractals only on micropores larger than 0.60 nm.

The calculated D_{s2} values range from 2.77 to 2.95, demonstrating clear fractal characteristics. The D_{s2} values for coal facies *A*, *B*, and *C* are 2.77–2.95, 2.84–2.86, and 2.83–2.86, respectively (Figure 10b). The D_{s2} values exhibit minimal variation among different coal facies types, indicating that coal facies has a limited effect on micropore development, a conclusion supported by Figure 5. However, the D_{s2} values of coal facies *A* (2.77–2.95) are larger than those of other types, suggesting that the samples in coal facies *A* have the strongest heterogeneity in the 0.6–1.2 nm pore distribution range.

3.2.3 Multi-fractal analysis based on CO_2 adsorption curves

The single fractal cannot fully characterize the heterogeneity differences of micropores. In this article, the $q \sim D$ fractal dimension spectrum is selected to describe the multifractal results. Taking the sample M-2 as an example, the relationship between $\lg(x(q, \varepsilon))$ and $\lg(\varepsilon)$ was studied (Figure 11a). There is a good linear relationship between q and $i(q)$ (Figure 11b), and as q increases $i(q)$ increases monotonically, illustrating multi-fractal behavior in micropore size distribution. Significant differences in $D_0 - D_{10}$ and $D_{-10} - D_0$ among all samples indicate substantial variations in pore volumes within the micropore range (Figure 11c, d, and f). $D_0 - D_{10}$ exhibits less variation among all samples, whereas $D_{-10} - D_0$ displays more variability among different coal facies types. Specifically, $D_{-10} - D_0$ for coal facies *A*, *B*, and *C* ranges from 0.1 to 0.22, 0.09 to 0.16, and 0.12 to 0.18, respectively.

D_{-10} (1.13–1.15) and D_{10} (0.97–0.98) exhibit less variation among all samples (Figure 12a and b). The values of $D_{-10} - D_0$ and $D_0 - D_{10}$ are larger for coal facies *A* compared to other types, suggesting stronger heterogeneity in micropore distribution in both the low- and high-pore-volume development areas of this coal facies (Figure 12c and d). $D_{-10} - D_{10}$ of coal facies *A* is 1.1–1.22 (Figure 12e), surpassing other types, further emphasizing the stronger heterogeneity in micropore distribution for coal facies *A*.

As $D_{-10} - D_0$ increases, $D_{-10} - D_{10}$ increases linearly with an R^2 of 0.98, and $D_0 - D_{10}$ increases similarly (Figure 13a), indicating that the lower pore volume area controls the heterogeneity of the micropore size distribution. The volume percentage of pores smaller than 0.55 nm increases progressively with $D_{-10} - D_0$, and the heterogeneity of the micropore size distribution is impacted by pores smaller than 0.55 nm.

3.3 Effect of coal facies on 2–100 nm pore heterogeneity

3.3.1 Mesopore distribution of samples of different coal facies types

The N_2 adsorption curve reflects the pore size distribution of mesopores. The total adsorption volume for coal facies *A* ranges from 0.71 to 8.64 $cm^3\ g^{-1}$, and that for coal facies *C* is

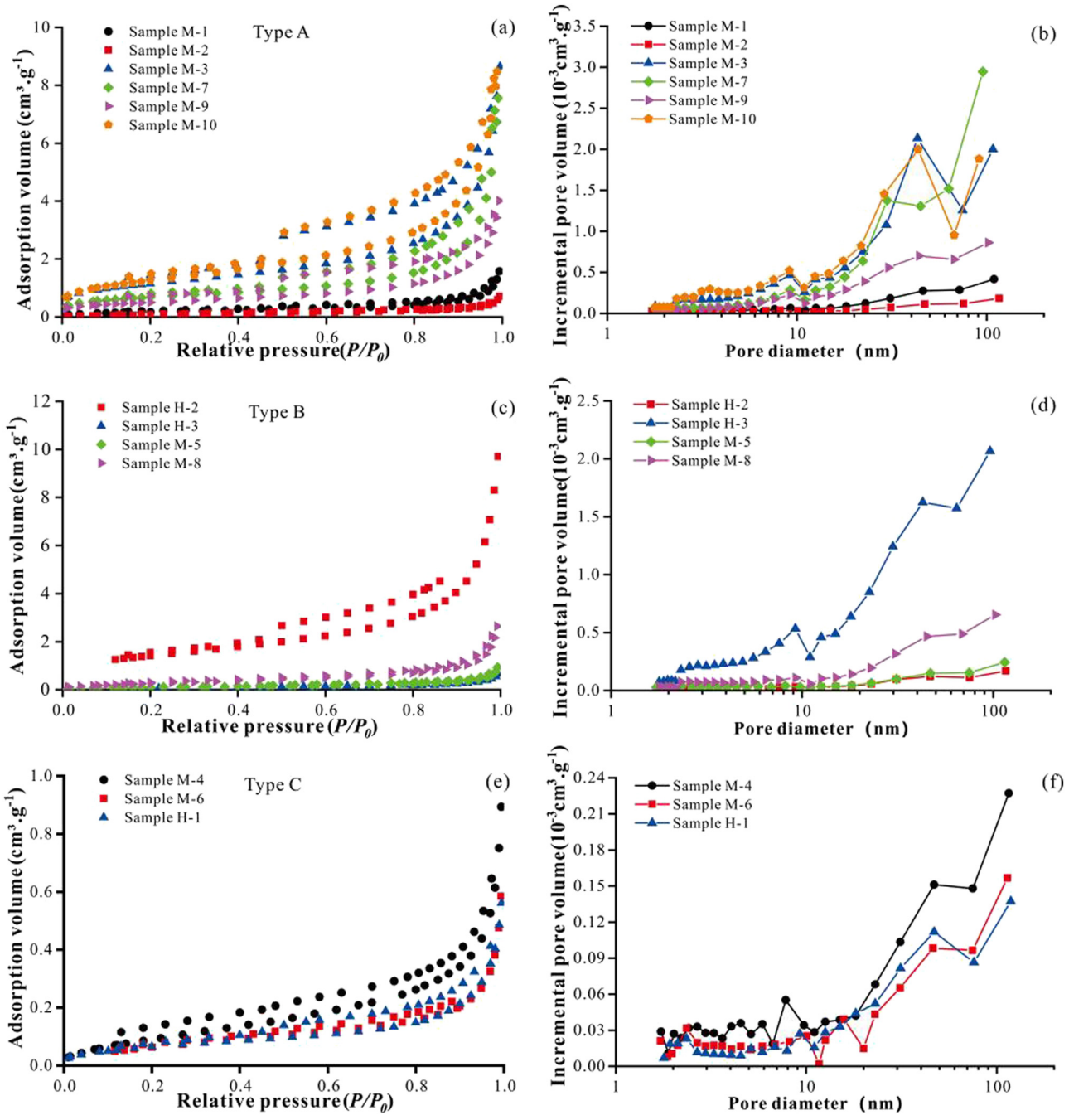

Figure 14: N_2 adsorption curves of coal samples (a, c, e) and mesopore size distribution of different coal facies samples (b, d, f).

0.56–0.89 $cm^3\ g^{-1}$ (Figure 14a, c and e). Coal facies *A* exhibits separated adsorption–desorption curves with clear hysteresis loops (except for sample M-2), suggesting the development of ink-bottle pores with a more complex pore structure. Conversely, coal facies *C* displays coinciding adsorption–desorption curves, indicating well-developed open pores are a simpler pore structure. Coal facies *B*, represented by varying adsorption and desorption curve morphologies, shows obvious hysteresis loops and ink-bottle pores in samples H-2 and H-3, while samples M-5 and M-8 display open pores. Coal facies *B* samples are in a transitional stage between coal facies *A* and *C*, exhibiting relatively complex variations (Figure 14a, c, and e). Two peaks are shown in mesopore distribution curves at about 10 nm and 45 nm (Figure 14b, d, and f).

The pore volume and specific surface area of mesopores are the largest for coal facies *A* (0.007 $cm^3\ g^{-1}$ and

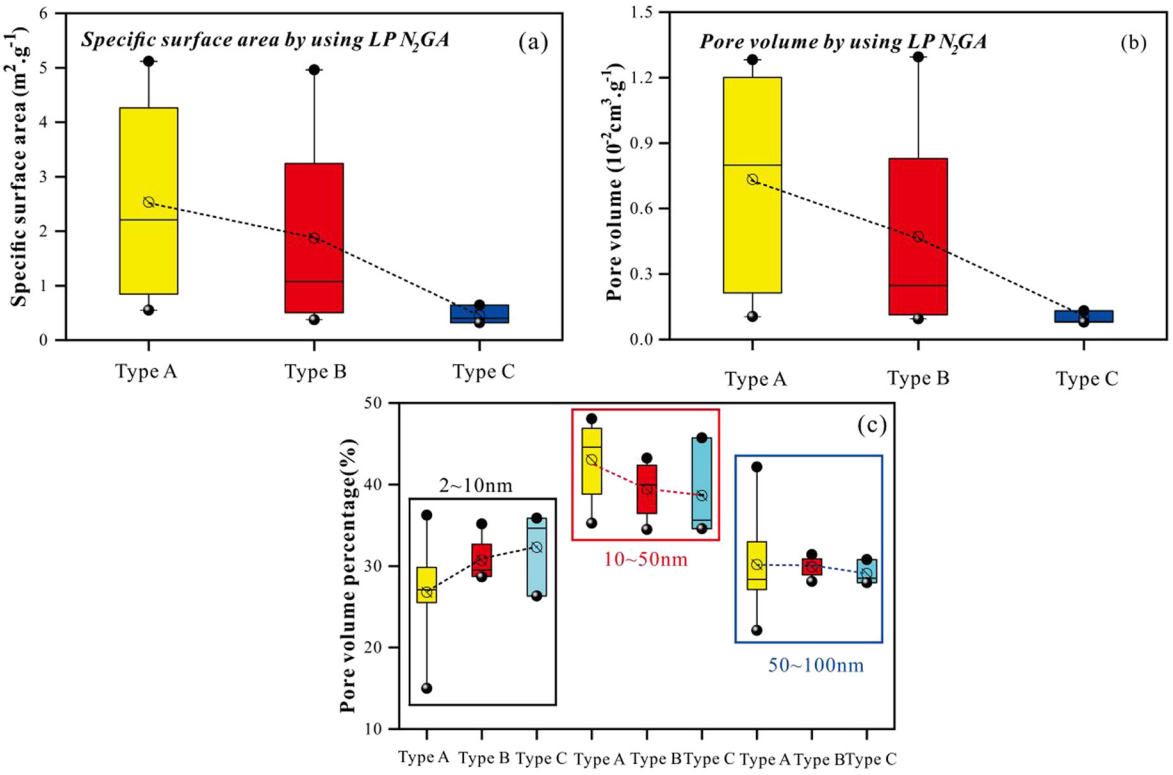

Figure 15: Comparison of mesopore structural parameters among different coal facies samples. Specific surface area of different coal facies types (a), pore volume of different coal facies types (b), and pore volume percentage of different coal facies types (c).

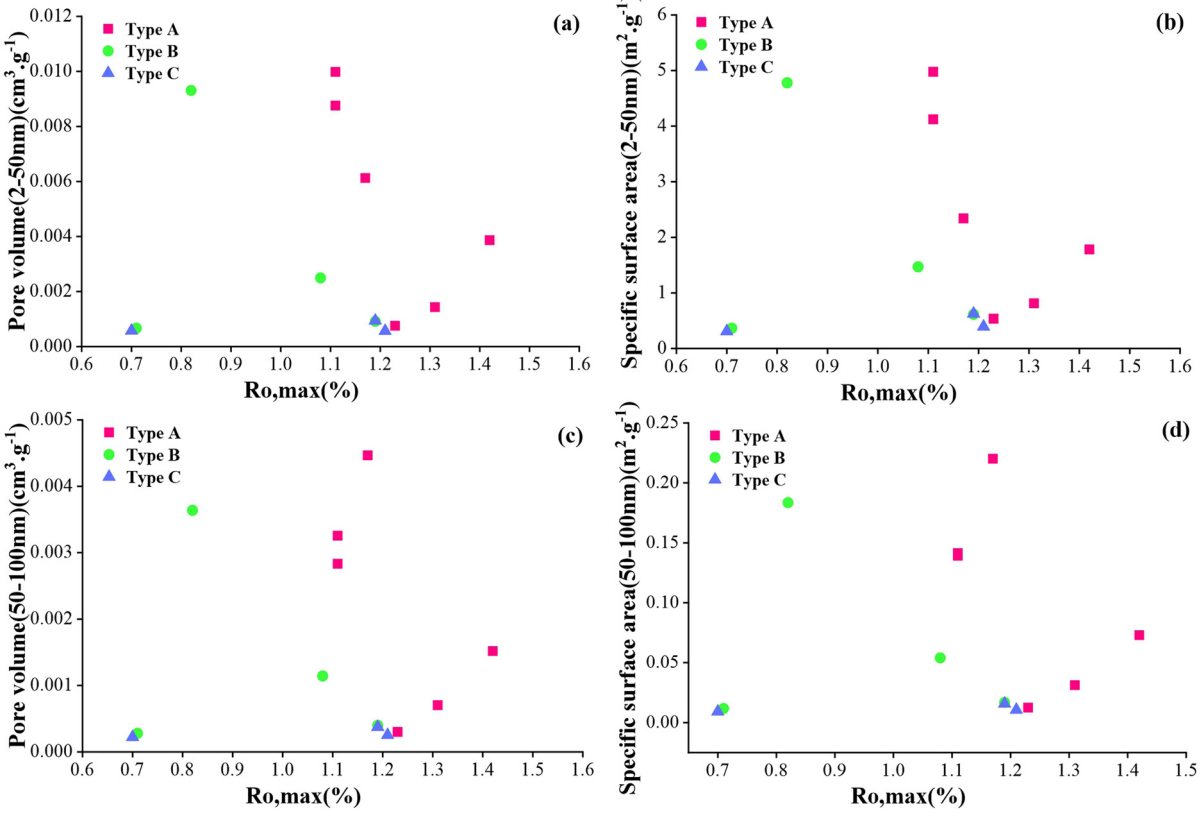

Figure 16: Relationship between mesopore volume and $R_{o,\ max}$. Crossplots of $R_{o,\ max}$ and pore volume (a, c) and crossplots of $R_{o,\ max}$ and specific surface area (b, d).

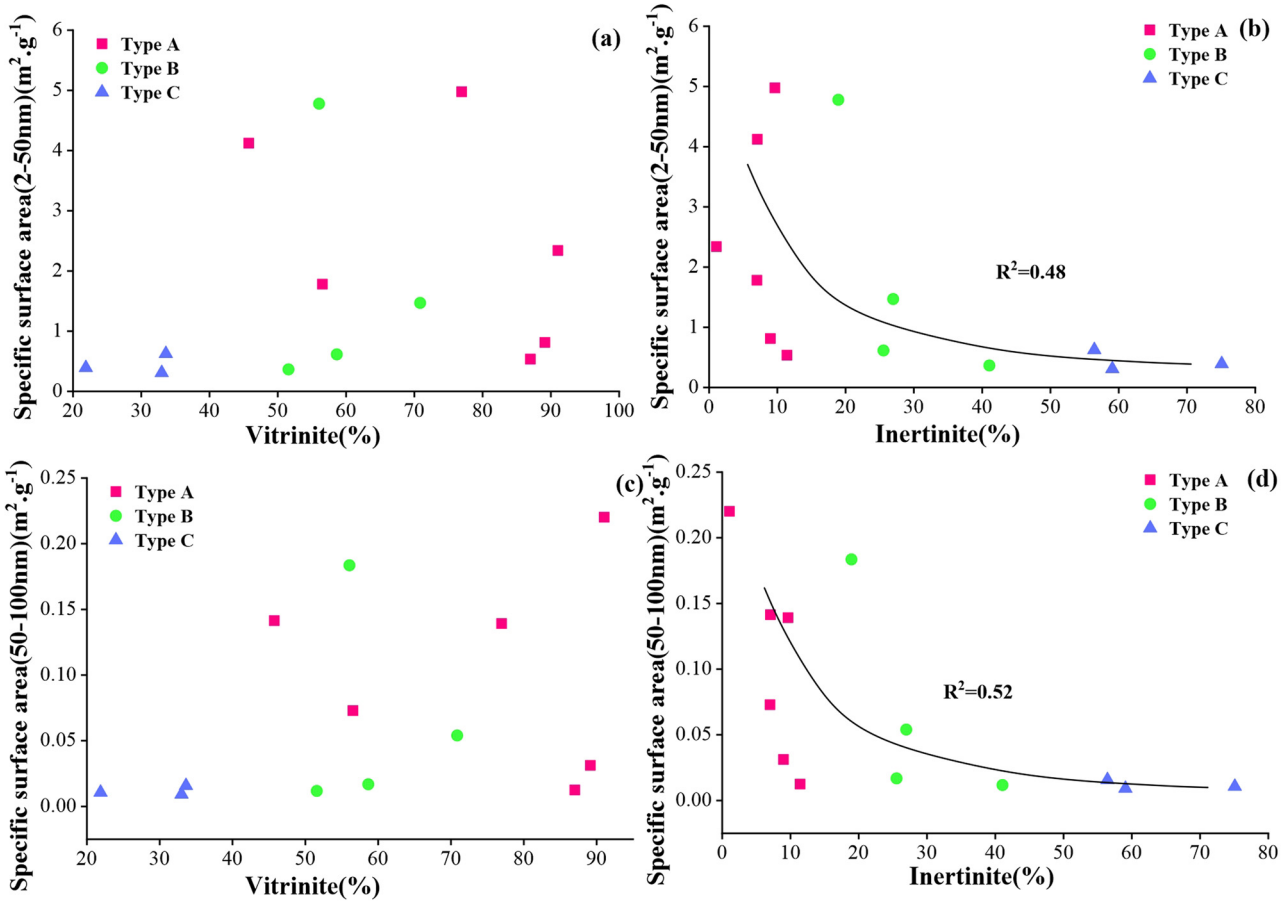

Figure 17: Relationship between mesopore-specific surface area and vitrinite (a, c), and relationship between mesopore-specific surface area and inertinite (b, d).

2.5 $m^2 g^{-1}$), indicating the most developed mesopores in coal facies *A* (Figure 15a and b). The percentage of pore volume with a diameter of 2–10 nm in coal facies *A* is the lowest among the three coal facies, whereas the volume percentage of 10–50 nm pores in coal facies *A* is much higher than that of other coal facies (Figure 15c). These results underscore the influence of coal facies type on mesoporous structure development.

Compared to micropores (Figure 8), the pore volume and specific surface area of 2–100 nm pores show a weaker correlation with $R_{o,max}$ (Figure 16). It is suggested that the pore structure within this range is influenced not only by coal maturity but also by fundamental coal parameters such as moisture and ash content, making the structural variations of these pores more complex than those of micropores.

The specific surface area of 2–50 nm and 50–100 nm pores shows a weak correlation with vitrinite content (Figure 17a and c), while a certain correlation exists with inertinite content. As inertinite content increases, the specific surface area of the pores decreases (Figure 17b and d). Compared to coal facies *A*, coal facies *B* and *C* have higher inertinite content, fewer micropores, poorer adsorption capacity, and more developed mesopores and macropores, resulting in higher permeability. This indicates that inertinite plays a controlling role in coal reservoirs where meso- and macropores are predominant.

3.3.2 Single-fractal analysis based on N_2 adsorption and desorption curves

The N_2 adsorption curve is employed to examine the mesopore fractal dimension, with limited studies conducted on the fractal dimension of the desorption curve. It was found that the fractal values obtained by the liquid nitrogen desorption curve are also physically meaningful [33]. Utilizing the FHH model, all coal samples are subjected to a single fractal, and the fractal dimension is calculated (Figure 18). Figure 18 shows that the two sections of the fractal curves are roughly circumscribed by P/P_0 = 0.5, which corresponds to a pore size of 4 nm.

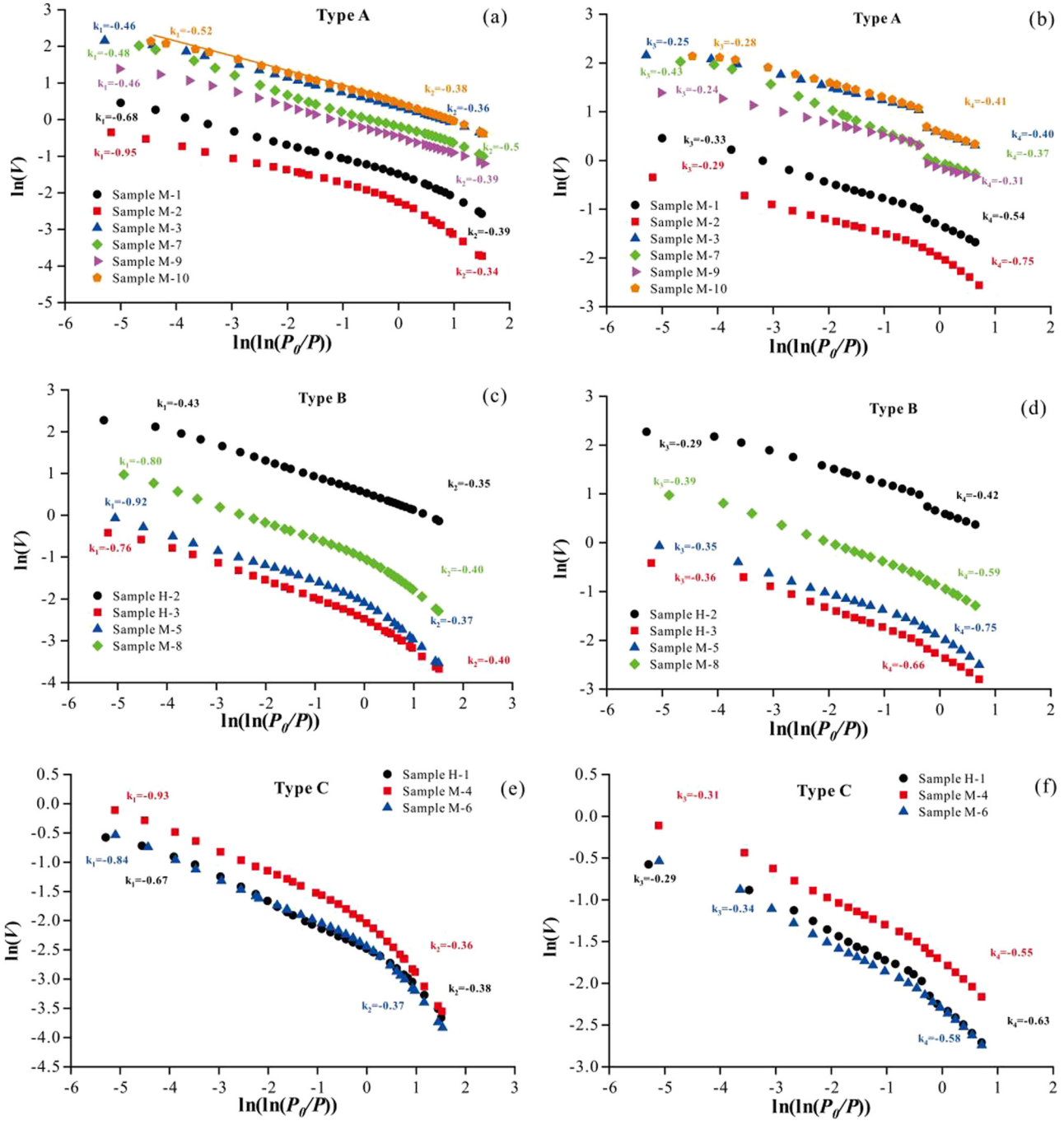

Figure 18: Fractal curves of mesopores using N_2 adsorption desorption data (a, c, e) and N_2 desorption data (b, d, f).

The single fractal dimension contains four parameters in each coal sample, i.e., D_1 (P/P_0 < 0.5, in the adsorption curve), D_2 (P/P_0 > 0.5, in the adsorption curve), D_3 (P/P_0 > 0.5, in the desorption curve), and D_4 (P/P_0 < 0.5, in the desorption curve). The fractal dimension values are the following: D_1 = 2.05–2.71, D_2 = 2.37–2.66, D_3 = 2.57–2.76, and D_4 = 2.25–2.69. These values fall within the defined fractal range of 2–3, indicating clear fractal characteristics across the entire pressure range.

Previous research has demonstrated that the fractal dimension value obtained by P/P_0 < 0.5 represents the heterogeneity of pore volume and reflects the pore space morphology [34]. Similarly, values obtained for P/P_0 > 0.5 also represent the heterogeneity of pore surface area and reflect the pore surface morphology. Compared to coal facies *B* and *C*, the fractal curves of coal facies *A* are nearly straight lines, indicating consistent heterogeneity in the mesopore distribution of coal facies *A* samples (Figure 18a,

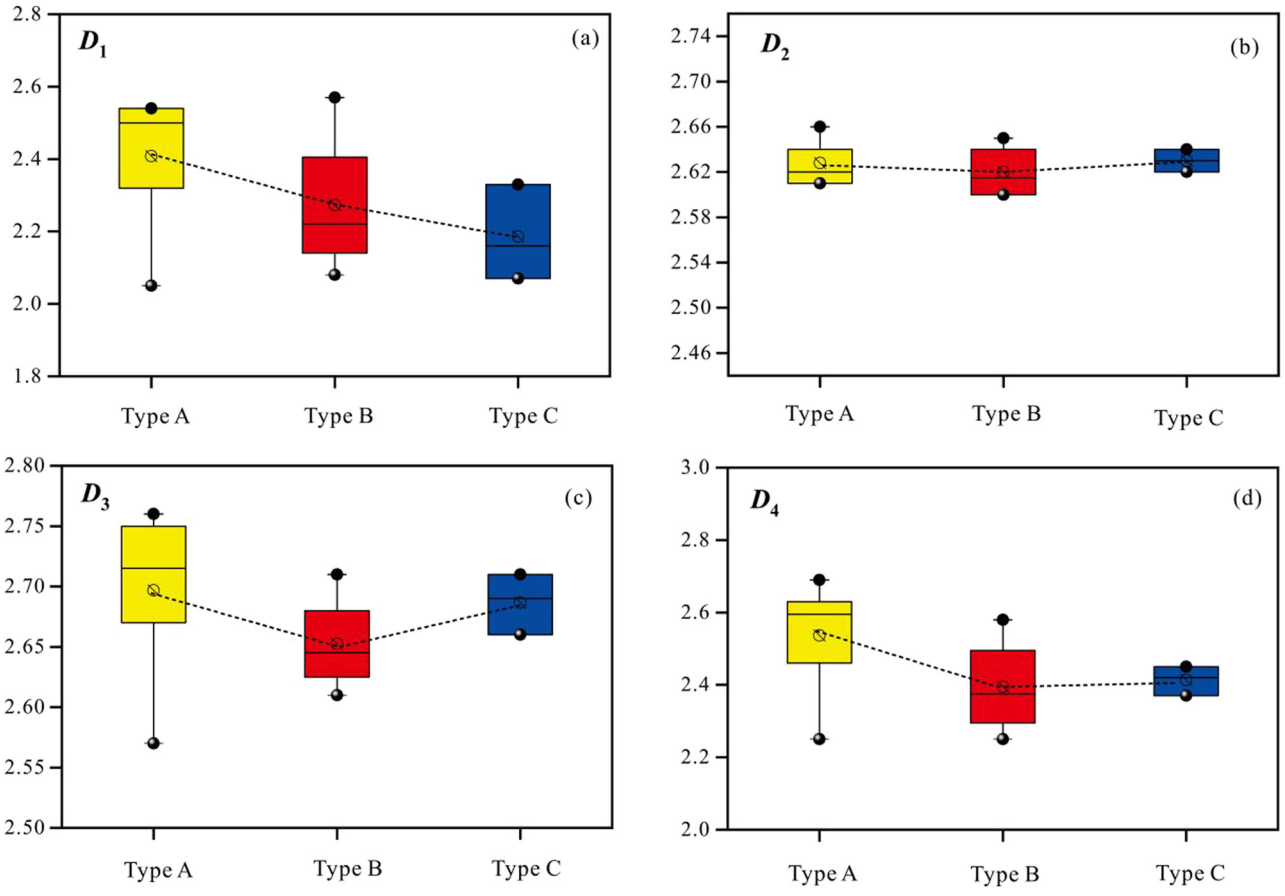

Figure 19: D_1 values of different coal facies types (a), D_2 values of different coal facies types (b), D_3 values of different coal facies types (c), D_4 values of different coal facies types (d).

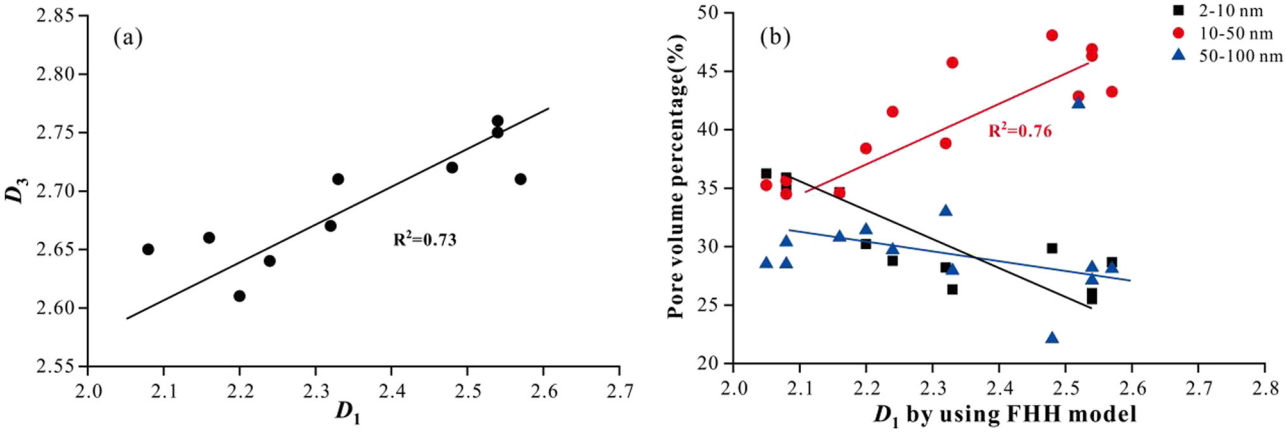

Figure 20: Multi-fractal dimension correlation. The relationship between D_1 and D_3 (a), relationship between D_1 and pore volume percentage (b).

c, and e). The fractal slopes obtained from the desorption curves range between −0.75 and −0.25, indicating fractal significance (Figure 18b, d, and f). The four parameters of coal facies *A* are larger than those of the other two coal facies, which indicates that the heterogeneity of mesopore restricted by coal facies *A* is the strongest (Figure 19).

A linear positive correlation exists between D_1 and D_3 (R^2 = 0.73), indicating that the liquid nitrogen desorption curve conforms to the fractal condition and exhibits fractal significance (Figure 20a). Additionally, D_1 and the volume percentage of pores with 10–50 nm have a linearly positive association. (Figure 20b), indicating that the mesopore distribution

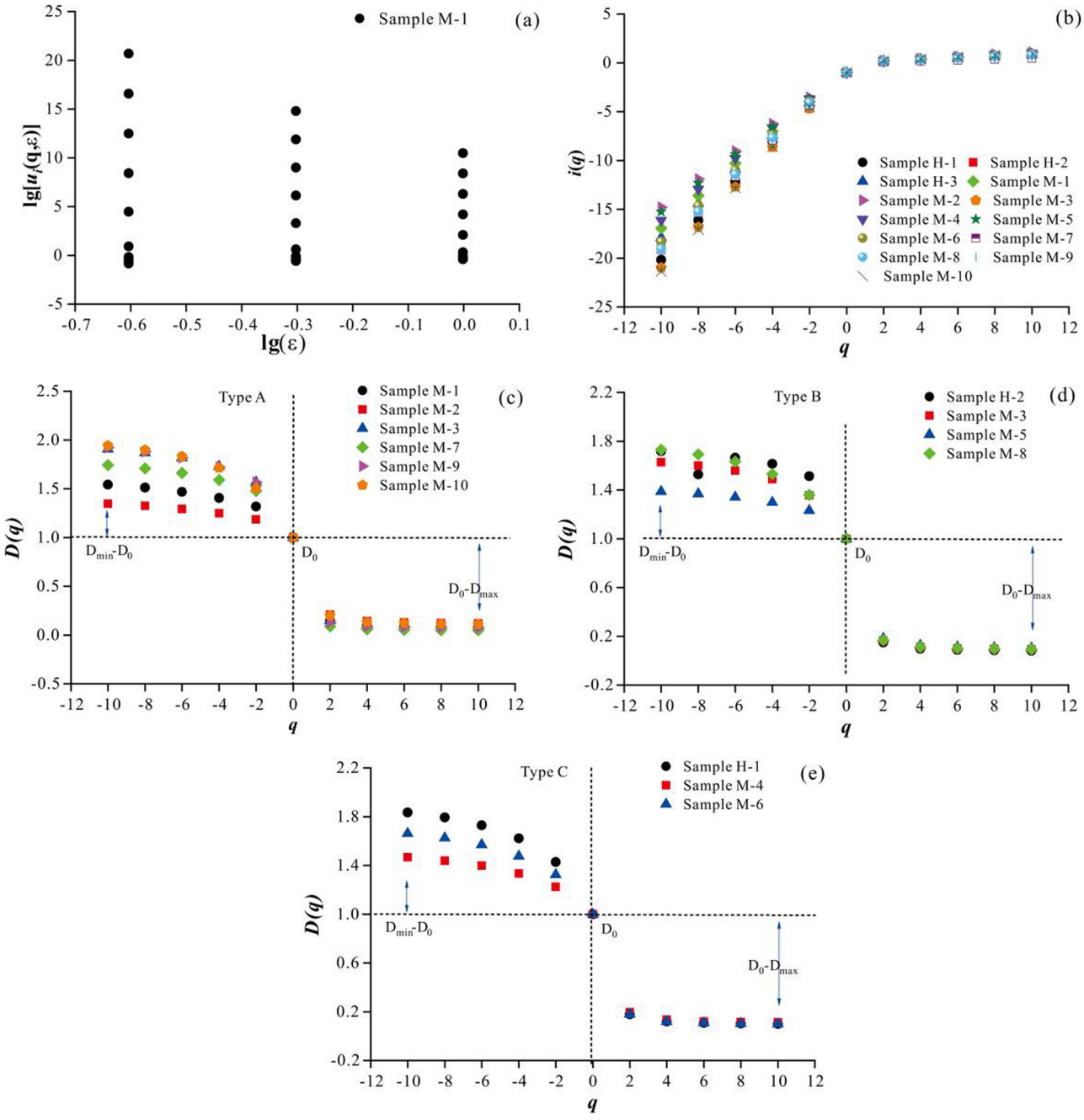

Figure 21: Multifractal curves characteristics of mesopores. The linear relationship between *q* and *i(q)* (a, b), and the linear relationship between *q* and *D(q)* in different coal facies types (c–e).

heterogeneity is regulated by pores of 10–50 nm. This also indicates that D_1 reflects the volume roughness of the pore structure, aligning with previous experimental observations [35].

3.3.3 Multi-fractal analysis based on N_2 adsorption and desorption curves

Taking the sample M-1 as an example, the relationship between lg($x(q, \varepsilon)$) and lg(ε) was studied. When $q < 0$, $i(q)$ increases with an increase of q, while when $q > 0$, the increase of $i(q)$ is not obvious (Figure 21b). This pattern suggests a multi-fractal behavior in mesopore size distribution. $D_0 - D_{10}$ and $D_{-10} - D_0$ showed significant differences across all samples, indicating substantial variations in mesopore volumes. $D_{-10} - D_0$ varies more among different coal facies, with $D_{-10} - D_0$ values for coal facies *A*, *B*, and *C* ranging from 0.34 to 0.94, 0.39 to 0.74, and 0.47–0.83, respectively (Figure 21c, d and f).

In the low-value zone of pore volume, a larger $D_{min} - D_0$ indicates stronger heterogeneity. In addition, in the

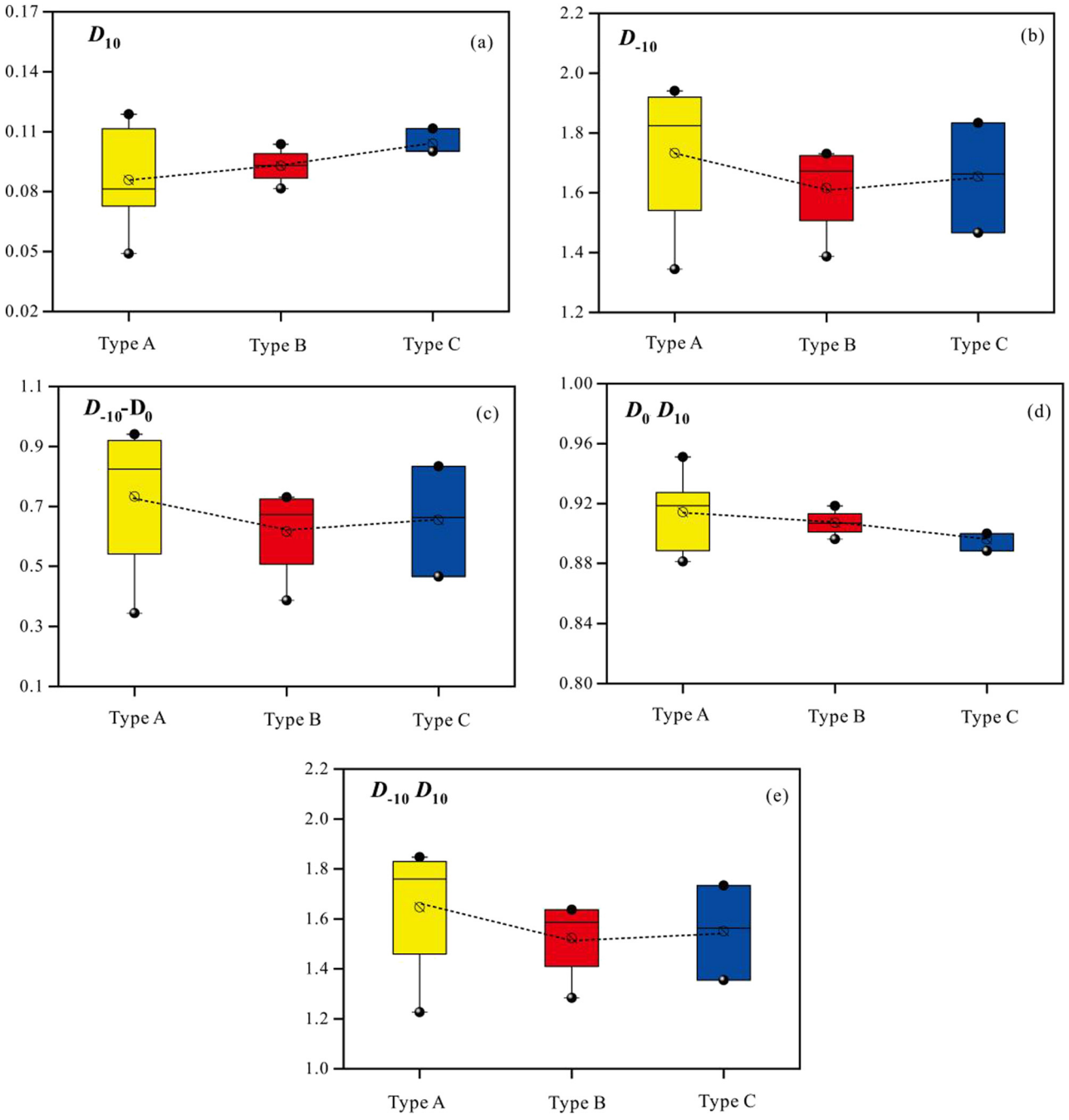

Figure 22: Comparison of multi-fractal parameters in different coal facies types. D_{10} and D_{-10} of different coal facies types (a, b), the relationship between D_{10}, D_{-10} and D_0 (c–e).

high-value zone, increasing $D_0 - D_{10}$ indicates stronger heterogeneity in pore size distribution. D_{10} (0.085–0.105) for the coal facies types show minimal differences, with the D_{-10} of coal facies *A* higher than that of coal facies *B* and *C* (Figure 22a and b). These results suggest that the mesopore distribution in coal facies *B* and *C* is more homogeneous compared to coal facies *A*. The $D_{-10} - D_0$ and $D_0 - D_{10}$ of coal facies *A* are the largest compared to coal facies *B* and *C*, suggesting that coal facies *A* is more heterogeneous in the pore-volume low-value zone and the pore volume of the high-value zone (Figure 22c and d). Figure 22e shows that the $D_{-10} - D_{10}$ of coal facies *A* is 2–8 (larger than other types), indicating an overall stronger heterogeneity of mesopore distribution.

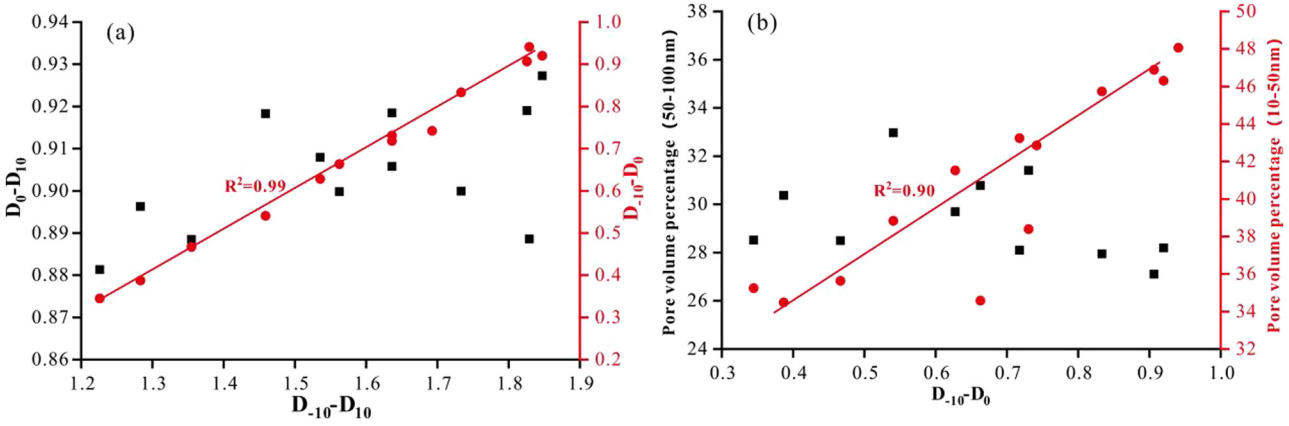

Figure 23: Correlation between multi-fractal parameters. Plots of $D_{-10} - D_{10}$ and $D_0 - D_{10}$ (a), the relationship between $D_{-10} - D_0$ and pore structure parameters (b).

As $D_{-10} - D_0$ increases, $D_{-10} - D_{10}$ increases linearly with an R^2 of 0.99 (Figure 23a), indicating that the heterogeneity of the mesopore distribution is primarily governed by the lower pore volume area. Furthermore, $D_{-10} - D_0$ gradually increases with an increase in the volume percentage of pores of 10–50 nm, indicating that pores of 10–50 nm play a significant role in governing the heterogeneity of mesopores.

4 Conclusions

In this study, coal facies were identified based on maceral characteristics. The micropore and mesopore size distribution of different coal samples was quantitatively characterized by low-temperature liquid nitrogen and carbon dioxide adsorption tests. Subsequently, the difference in volume and specific surface area distributions of nanopores in different coal facies samples were discussed. The heterogeneity of micropore and mesopore distributions was investigated. Eventually, the differences in the pore structures in different coal facies samples were clarified. The key findings are summarized as follows.

(1) All coal samples can be categorized into three coal facies types: low marsh reed phase (A, GI > 5, TPI < 1), wetland grassy swamp phase (B, GI < 5, TPI < 1), and dry forest swamp phase (C, GI < 1, TPI > 1).
(2) Low-temperature liquid nitrogen tests show that the coal facies controls the development characteristics of mesopores, with mesopore volume following the order: coal facies *A* > coal facies *B* > coal facies *C*, and mesopore specific surface area following the order: coal facies *A* > coal facies *B* > coal facies *C*.
(3) Single-fractal analysis based on the N_2 adsorption–desorption curve and CO_2 adsorption curve show that the liquid nitrogen desorption curve conforms to the fractal conditions and exhibits fractal significance. Different fractal dimensions indicated that the coal facies *A* have the strongest heterogeneity.
(4) Utilizing the multiple fractal theory to quantitatively characterize the heterogeneity of the pore structure, the multiple fractals results indicate that the heterogeneity of mesopores is regulated by pores of 10–50 nm, and pores smaller than 0.55 nm affect the heterogeneity of the micropore size distribution.
(5) The coal reservoir under the wet overlying water depositional environment of coal facies *A* offers a relatively large pore volume as well as specific surface area, which is more favorable for the exploration and development of coalbed methane; therefore, it is the advantageous coal reservoir in the study area.

Acknowledgements: The authors are grateful for the reviewer's valuable comments that improved the manuscript. The datasets generated during and/or analysed during the current study are available from the corresponding author on reasonable request.

Funding information: This study was funded by the National Natural Science Foundation of China (Grant Nos 42072172 and 42372160).

Author contributions: Conceptualization: ZLY; methodology: CXC, ZJJ; formal analysis and investigation: ZLY, YP, LDJ, and SJT; writing – original draft preparation: ZLY; writing – review and editing: VV, CXC, and ZJJ; funding acquisition: CXC.

Conflict of interest: The authors declare that they have no known competing financial interests or personal relationships that could have appeared to influence the work reported in this paper.

References

[1] Zhao L, Qin Y. Control of coal facies to adsorption-desorption divergence of coals: A case from the Xiqu Drainage Area, Gujiao CBM Block, North China. Int J Coal Geol. 2017;171:169–84. doi: 10.1016/j.coal.2017.01.006.

[2] Zhai Y. The characteristics of coal facies in the Permian coal seams in the north of pingdingshan and its control of coal pore characteristics. Master's thesis. Henan Polytechnic University; 2022.

[3] Clara G, Marco R, Mauricio AB. Relationship between coal composition, coal facies, and desorbed methane gas content: Thermal histories and exhumation processes in the middle Magdalena Valley basin, Colombia. J South Am Earth Sci. 2023;128:104369. doi: 10.1016/j.jsames.2023.104369.

[4] Li T, Wu C, Liu Q. Characteristics of coal fractures and the influence of coal facies on coalbed methane productivity in the South Yanchuan Block, China. J Nat Gas Sci Eng. 2015;22:625–32. doi: 10.1016/j.jngse.2015.01.014.

[5] Shen Y, Wang X, Shi Q. Coal facies characteristics and pore structure response of oil-rich coal in Yushenfu Mining Area. Saf Coal Mines. 2021;52(10):30–37+44. doi: 10.13347/j.cnki.mkaq.2021.10.007.

[6] Jin K, Cheng Y, Liu Q. Experimental investigation of pore structure damage in pulverized coal: Implications for methane adsorption and diffusion characteristics. Energy Fuels. 2016;30(12):10383–95. doi: 10.1021/acs.energyfuels.6b02530.

[7] Xi K, Cao Y, Liu K, Jahren J, Zhu R, Yuan G, et al. Authigenic minerals related to wettability and their impacts on oil accumulation in tight sandstone reservoirs: An example from the Lower Cretaceous Quantou Formation in the southern Songliao Basin, China. J Asian Earth Sci. 2019;178:173–92. doi: 10.1016/j.jseaes.2018.04.025.

[8] Xi K, Cao Y, Liu K, Wu S, Yuan G, Zhu R, et al. Geochemical constraints on the origins of calcite cements and their impacts on reservoir heterogeneities: A case study on tight oil sandstones of the Upper Triassic Yanchang Formation, southwestern Ordos Basin, China. AAPG Bull. 2019;103(10):2447–85. doi: 10.1306/01301918093.

[9] Guo H, Wang K, Cui H. Experimental iovestioation on the pore and fracture structure of the reconstructed coal and its fractal characteristics. J China Univ Min Technol. 2019;48(6):1206–14.

[10] Zhao Z, Liu P, Li Q, Nie B, Zhao K, Zhao Y, et al. Evaluating coal pore structure and gas sorption-diffusion behavior alteration induced by ultrasound stimulation using sorbing tests and matrix diffusion modeling. Geoenergy Sci Eng. 2024;234:212642. doi: 10.1016/j.geoen.2024.212642.

[11] Li L, Liu D, Cai Y, Wang Y, Jia Q. Coal structure and its implications for coalbed methane exploitation: a review. Energy Fuels. 2021;35(1):86–110. doi: 10.1021/acs.energyfuels.0c03309.

[12] Fan Q, Cai Y, Bei J. Pore and fracture structure of coal reservoir constrained by coal metamorphism. Geoscience. 2020;34(2):273–80.

[13] Lou Y, Su Y, Wang W, Xia P. Coal facies and its effects on pore characteristics of the Late Permian Longtan coal, Western Guizhou, China. Geofluids. 2022;2022(1):6071514. doi: 10.1016/j.fuel.2020.118248.

[14] Ou C, Li C, Rui Z, Ma Q. Lithofacies distribution and gas-controlling characteristics of the Wufeng–Longmaxi black shales in the southeastern region of the Sichuan Basin, China. J Pet Sci Eng. 2018;165:269–83. doi: 10.1016/j.petrol.2018.02.024.

[15] Li J, Lu S, Chen G, Wang M, Tian S, Guo Z. A new method for measuring shale porosity with low-field nuclear magnetic resonance considering non-fluid signals. Mar Pet Geol. 2019;102:535–43. doi: 10.1016/j.marpetgeo.2019.01.013.

[16] Xue C, Wu J, Qiu L, Zhong J, Zhang S, Zhang B, et al. Lithofacies classification and its controls on the pore structure distribution in Permian transitional shale in the northeastern Ordos Basin, China. J Pet Sci Eng. 2020;195:107657. doi: 10.1016/j.petrol.2020.107657.

[17] Cai Y, Liu D, Yao Y, Li J, Liu J. Fractal characteristics of coal pores based on classic geometry and thermodynamics models. Acta Geol Sin (English Edition). 2011;85(5):1150–62. doi: 10.1111/j.1755-6724.2011.00247.x.

[18] Zhao Z, Liu G, Chang P, Wang X, Lin J. Fractal characteristics for coal chemical structure: Principle, methodology and implication. Chaos, Solitons Fractals. 2023;173:113699. doi: 10.1016/j.chaos.2023.113699.

[19] Liu X, Nie B. Fractal characteristics of coal samples utilizing image analysis and gas adsorption. Fuel. 2016;182(1):314–22. doi: 10.1016/j.fuel.2016.05.110.

[20] Li Z, Ren T, Li X, Qiao M, Yang X, Tan L, et al. Multi-scale pore fractal characteristics of differently ranked coal and its impact on gas adsorption. Int J Min Sci Technol. 2023;33:389–401. doi: 10.1016/j.ijmst.2022.12.006.

[21] Wang K, Yang H, Li Y, Zhang R, Ma Y, Wang B. Geological characteristics and exploration potential of the northern tectonic belt of Kuqa depression in Tarim Basin. ACTA Petrolei Sin. 2021;42(7):885–905. doi: 10.7623/syxb202107005.

[22] Zhao G, Li X, Liu M, Dong C, Li J, Liu Y, et al. Fault activity and hydrocarbon accumulation significance of structural belt in northern Kuqa Depression. J Min Sci Technol. 2022;7(1):34–44. doi: 10.19606/j.cnki.jmst.2022.01.004.

[23] Diessel CFK. The correlation between coal facies and depositional environments. In Proceedings of 20th Symposium. The University of Newcastle, Newcastle; 1986. p. 19–22.

[24] Calder JH, Gibling MR, Mukhopadhyay PK. Peat formation in a Westphalian B piedmont setting, Cumberland Basin, Nova Scotia: implications for the maceral based interpretation of rheotrophic and raised paleomires. Bull Soc Géol Fr. 1991;162(2):283–98.

[25] Diessel CFK. Utility of coal petrology for sequence-stratigraphic analysis. Int J Coal Geol. 2007;70(1–3):3–34. doi: 10.1016/j.coal.2006.01.008.

[26] Ahmad AL, Mustafa NNN. Pore surface fractal analysis of palladium-alumina ceramic membrane using Frenkel-Halsey-Hill (FHH) model. J Colloid Interface Sci. 2006;301(2):575–84. doi: 10.1016/j.jcis.2006.05.041.

[27] Yao P, Zhang J, Lv D, Veerle V, Chang X. Effect of water occurrence in coal reservoirs on the production capacity of coalbed methane by using NMR simulation technology and production capacity simulation. Geoenergy Sci Eng. 2024;243:213353. doi: 10.1016/j.geoen.2024.213353.

[28] Paz Ferreiro J, Vidal Vázquez E. Multifractal analysis of Hg pore size distributions in soils with contrasting structural stability. Geoderma. 2010;160(1):64–73. doi: 10.1016/j.geoderma.2009.11.019.
[29] Zhao P, Wang X, Cai J, Luo M, Zhang J, Liu Y, et al. Multifractal analysis of pore structure of Middle Bakken formation using low temperature N2 adsorption and NMR measurements. J Pet Sci Eng. 2019;176:312–20. doi: 10.1016/j.petrol.2019.01.040.
[30] Liu K, Ostadhassan M, Zou J, Gentzis T, Rezaee R, Bubach B, et al. Multifractal analysis of gas adsorption isotherms for pore structure characterization of the Bakken Shale. Fuel. 2018;219:296–311. doi: 10.1016/j.fuel.2018.01.126.
[31] Friesen WI, Mikula RJ. Mercury porosimetry of coals: pore volume distribution and compressibility. Fuel. 1987;67:1516–20. doi: 10.1016/0016-2361(88)90069-5.
[32] Posnansky O, Guo J, Hirsch S, Papazoglou S, Braun J, Sack I. Fractal network dimension and viscoelastic powerlaw behavior: I. A modeling approach based on a coarse-graining procedure combined with shear oscillatory rheometry. Phys Med Biol. 2012;57:4023–41. doi: 10.1088/0031-9155/57/12/4023.
[33] Zhang J, Wei C, Chu X, Vandeginste V, Ju W. Multifractal analysis in characterizing adsorption pore heterogeneity of middle- and high-rank coal reservoirs. ACS Omega. 2020;5(31):19385–19401. doi: 10.1021/acsomega.0c01115.
[34] Zhu J, Liu J, Yang Y, Cheng J, Zhou J, Cen K. Fractal characteristics of pore structures in 13 coal specimens: Relationship among fractal dimension, pore structure parameter, and slurry ability of coal. Fuel Process Technol. 2016;149:256–67. doi: 10.1016/j.fuproc.2016.04.026.
[35] Zhao J, Xu H, Tang D, Mathews JP, Li S, Tao S. A comparative evaluation of coal specific surface area by CO2 and N2 adsorption and its influence on CH_4 adsorption capacity at different pore sizes. Fuel. 2016;183:420–31.